
Knowledge-enhanced Visual-Language Pre-training on Chest Radiology Images

Xiaoman Zhang^{1,2}, Chaoyi Wu^{1,2}, Ya Zhang^{1,2}, Yanfeng Wang^{1,2}, Weidi Xie^{1,2}

¹Cooperative Medianet Innovation Center, Shanghai Jiao Tong University

²Shanghai AI Laboratory

{xm99sjtu, wtzxxxwcy02, ya_zhang, wangyanfeng, weidi}@sjtu.edu.cn

Abstract

While multi-modal foundation models pre-trained on large-scale data have been successful in natural language understanding and vision recognition, their use in medical domains is still limited due to the fine-grained nature of medical tasks and the high demand for domain knowledge. To address this challenge, we propose a novel approach called Knowledge-enhanced Auto Diagnosis (KAD) which leverages existing medical domain knowledge to guide vision-language pre-training using paired chest X-rays and radiology reports. We evaluate KAD on four external X-ray datasets and demonstrate that its zero-shot performance is not only comparable to that of fully-supervised models, but also superior to the average of three expert radiologists for three (out of five) pathologies with statistical significance. Moreover, when few-shot annotation is available, KAD outperforms all existing approaches in fine-tuning settings, demonstrating its potential for application in different clinical scenarios.

1 Introduction

Foundation models [6], such as, BERT [16], GPT [7] and CLIP [44] have shown great promise on feature transfer and generalisation to a wide spectrum of downstream tasks [37, 46, 14, 1], for example, in natural language processing or computer vision. However, the development of foundation models in medical domains has been largely lagged behind [44, 23, 61, 41]. A direct extension of existing approaches [63, 12] that align visual and text modalities in the medical domain hardly generalises towards diseases or radiology findings beyond those seen at training. This is largely due to the requirement for fine-grained recognition in medical tasks (*i.e.*, the clues for medical diagnosis often lie in subtle and regional signals), as well as the abstractness of many complex and professional medical terminologies (*e.g.*, infiltrates refers to the white spots in the lungs). Therefore, to effectively model the intricate and specialized concepts of medical applications, domain knowledge is indispensable.

In this paper, we aim to build a foundation model for chest X-rays by training on paired images and reports [29], termed as **Knowledge-enhanced Auto Diagnosis (KAD)**. As illustrated in Fig. 1, unlike existing approaches that simply align the image to raw textual reports, we investigate various ways to extract information from the given reports, and explicitly leverage a well-established medical knowledge graph to train knowledge encoder. In specific, the proposed KAD follows a two-stage framework, first, we learn a neural representation of knowledge graph, with the entities represented as nodes, and relations between them as edges, that offers scaffolds for structured, multi-step reasoning about entities; second, we extract the clinical entities and relations from radiology reports in three different ways, for example, by heuristically defined rules, by using RadGraph, or by using ChatGPT, then, we exploit the pre-trained knowledge encoder to guide the visual representation learning using image and radiology reports, effectively injecting the domain knowledge into visual encoder.

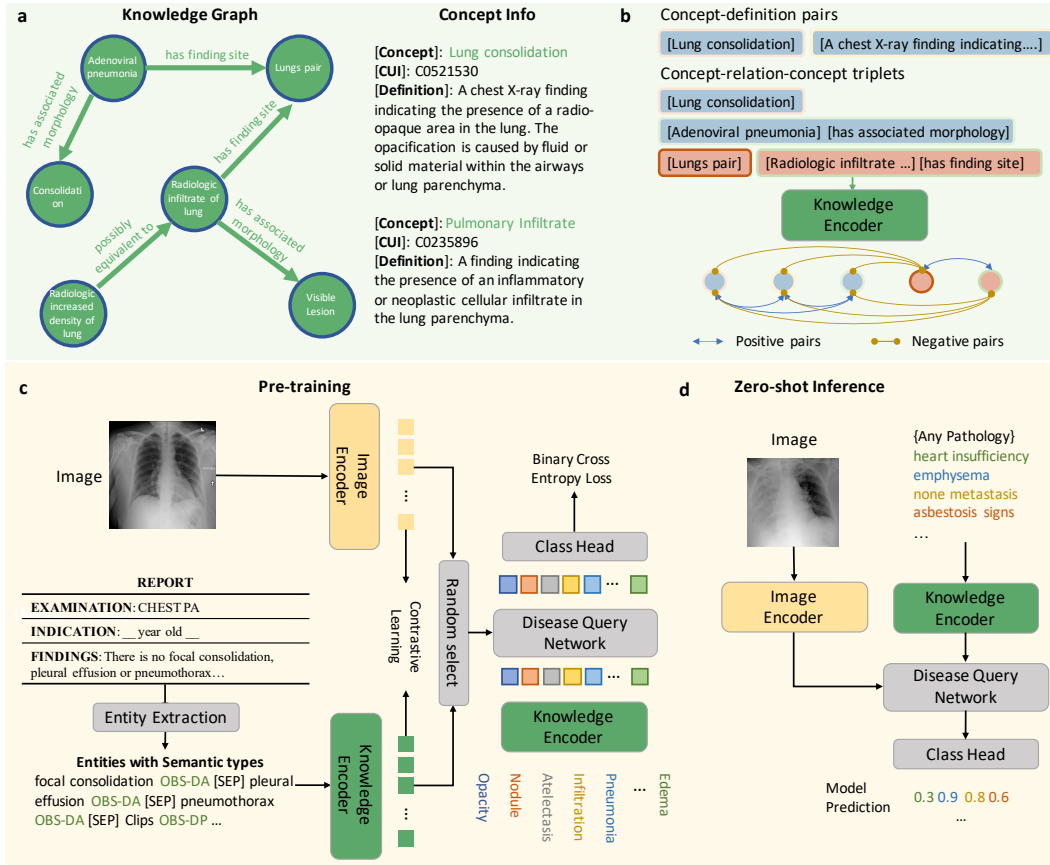


Figure 1: Overview of the KAD workflow. **a**, Knowledge base used for training the knowledge encoder. It contains two parts, knowledge graph consisting of concept-relation-concept triplets and concept info list consisting of concept-definition pairs. **b**, The knowledge encoder is trained to learn textual representations by maximizing similarities between positive pairs. **c**, We first extract the clinical entities and relations from the radiology reports, this can be achieved by heuristic rules, using an off-the-shelf reports information extraction toolbox (Entity Extraction), or ChatGPT, then we employ the pre-trained knowledge encoder to perform image-text contrastive learning with paired chest X-rays and extracted entities and optimize a Disease Query Network (DQN) for classification. **d**, During the inference stage, we simply encode the disease name as a query input, and DQN will output the probability that the pathology is present in the input image.

Architecturally, to enable flexible zero-shot evaluation on arbitrary diseases or radiology findings, we utilize a query-based transformer architecture, termed as Disease Query Network (DQN), that can take the disease name as ‘query’, iteratively attending the visual feature to get the model prediction, and the attention map provides reliable visual evidence for clinical decision.

To demonstrate the effectiveness of the proposed KAD, we experiment on four external X-ray datasets, *i.e.*, PadChest [8], ChestXray14 [53], CheXpert [26] and ChestX-Det10 [35]. KAD is shown to be superior in auto-diagnosis for pathologies that are unseen in the training procedure, with zero-shot performance significantly higher than existing state-of-the-art medical visual-language models for 193 pathologies on PadChest, and even comparable to the fully supervised approaches. To the best of our knowledge, this is the first model pre-trained with X-ray image and report, and demonstrate comparable or superior performance than the average for expert radiologists on CheXpert. In addition, when additional manual annotations are available, our model can also be fine-tuned in the same protocol as existing self-supervised learning methods, with further boosted performance, demonstrating its superior transferability. We believe that this work presents a promising idea for domain knowledge injection in developing foundation models for AI-assisted diagnosis in radiography.

2 Related Work

Vision-Language Pre-training Models. Vision-Language Pre-training (VLP) models have achieved great success in visual recognition. Generally, there are two typical structures for VLP models, *i.e.*, single-stream methods [32, 11] and two-stream methods [3, 30, 28]. In the medical domain, several approaches [61, 9, 23, 5, 55] have initiated the studies. ConVIRT [61] first proposed to use contrastive learning as a proxy task in medical. LoVT [9] and GLoRIA [23] then focus on improving the local alignment performance. BioViL [5] notices the language pattern in reports is different from other natural texts and re-designs the language model used for medical VLP. MedKLIP [55] proposed to leverage medical-specific knowledge, the disease descriptions to enhance representation learning. However, these studies suffer from limitations in knowledge incorporation and open-set generalization. Our work explicitly leverages a well-established medical knowledge graph into the self-supervised training procedure to address the above-mentioned limitations.

Medical Named-Entity-Recognition Models. Various natural language processing (NLP) approaches have been proposed to extract useful information from radiology reports [43, 26, 39, 47]. Recently, some analysis tools [4, 2] have been developed to extract key clinical concepts and their attributes from biomedical text. Other advanced works [27, 56] are further proposed to further extract relationships between different entities, which enables retaining most of the useful information in a structural format. This progress inspires us a lot and provides a new perspective for VLP. However, how to take advantage of these Named-Entity-Recognition (NER) models have not been discussed sufficiently in the VLP field.

Medical Knowledge Enhanced Models. Several efforts have attempted to leverage external medical knowledge to enhance deep learning models [57, 54]. The approaches can be classified into two types: model-based and input-based. In model-based approaches, one idea is to design models by imitating the radiological practice [31, 20, 52, 24] or change the model structure based on diagnostic patterns [40, 19, 13]. While in input-based approaches, the knowledge is treated as external inputs to calculate features [59, 58, 48] or to guide the final loss [10, 25]. Multi-task learning and attention mechanism [33, 34, 38] are often adopted to realize medical knowledge combination. In contrast to previous methods, we inject expert knowledge into the text embedding space by explicitly learning a neural representation of the medical knowledge graph, to provide knowledge guidance for representation learning on the visual side.

3 Method

3.1 Algorithm overview

At the core of our proposed idea is to train foundation models by leveraging the medical prior knowledge, in this paper, we explicitly leverage a well-established medical knowledge graph, *i.e.*, Unified Medical Language System (UMLS), and various information extraction methods, based on heuristic rules, RadGraph, or ChatGPT. Generally speaking, we train the model in two stages, first, we train a knowledge encoder to learn a neural representation of the medical knowledge base; second, we extract the clinical entities and relations from the radiology reports, and employ the pre-trained knowledge encoder to guide visual representation learning on image and text pairs of chest X-rays. In the following sections, we start by describing our considered problem scenario, and then present the detail of these two stages sequentially.

3.2 Problem scenario

Assuming a training set with N samples, *i.e.*, $\mathcal{D}_{\text{train}} = \{(x_1, t_1), \dots, (x_N, t_N)\}$, where x_i, t_i refer to the X-ray image and its corresponding medical report, respectively, our goal is to train a visual-language model that enables to diagnose the existence of any pathologies. Specifically, at inference time, we can freely ask the system to identify the likelihood of the patient getting a certain disease:

$$\hat{s}_i = \Phi_{\text{DQN}}(\Phi_{\text{image}}(x_i), \Phi_{\text{knowledge}}([\text{disease}])), \quad (1)$$

where $x_i \in \mathbb{R}^{H \times W \times 3}$ refers to an image sample from the test set, with H, W denoting height and width respectively, $\hat{s}_i \in [0, 1]$ refers to the inferred likelihood of the patient having a certain disease.

3.3 Knowledge encoder

In this section, we provide details for training the knowledge encoder ($\Phi_{\text{knowledge}}$), with experts’ knowledge to implicitly model the relations between medical entities in textual embedding space. Specifically, we employ contrastive learning to finetune a pre-trained BERT, by sampling positives and negatives from Unified Medical Language System (UMLS) [4].

Notation. Let $\mathcal{D}_{\text{UMLS}} = \{(n, c, d)_i\}_{i=1}^{|\mathcal{D}|}$ denote a concept dictionary for UMLS, each concept (n_i) has a Concept Unique Identifier (CUI, c_i) with corresponding definition (d_i) and Type Unique Identifier (TUI), as shown in Fig. 1. The concept “pulmonary infiltrate” is defined as “A finding indicating the presence of an inflammatory or neoplastic cellular infiltrate in the lung parenchyma”, and the corresponding CUI is C0235896. For the UMLS knowledge graph, the vertices are concepts ($\mathcal{D}_{\text{UMLS}}$), and each edge can be represented as a triplet, *i.e.*, (n_i, r, n_j) , where n_i refers to the head concept, n_j refers to the tail concept, and r refers to the relation from the head concept to the tail concept.

Training. Here, we train the knowledge encoder by maximizing the similarities between positive concept-definition pairs and concept-relation-concept triplets generated from the knowledge graph, such that the language description pointed to the same CUI have similar representations.

For a specific CUI c_i , the corresponding language descriptions may be expressed in three formats: the concept n_i , the definition d_i , and other concepts with the correct relationship $\{n_j + r\}$, r is the relationship between the head concept n_j pointing to tail concept n_i . **Note that**, there may exist more than one head concept pointing to the same tail concept, and we randomly select one of them for training. Given randomly N sampled CUIs, we can compute the textual embedding of corresponding language descriptions, *i.e.*, the concept $n_i \in \mathbb{R}^{N \times d}$, definition $d_i \in \mathbb{R}^{N \times d}$, and concepts with the relationship $\{n_j + r\} \in \mathbb{R}^{N \times d}$. Each pair of textual embeddings with same CUI can be treated as the positive, and the ones with different CUIs as negative pair.

At training time, for each CUI, we randomly sample **two** textual embeddings accordingly, and each mini-batch can be expressed as $\{(z_i, c_i)\}_{i=1}^{2N}$, where c_i denotes the CUI pointed by z_i . Here, we unify the textual embedding after knowledge encoder $\Phi_{\text{knowledge}}$ as z . Therefore, the model can be trained via contrastive learning by minimizing the distances between the z_i that points to the same CUI:

$$\mathcal{L}_{\text{knowledge}} = \sum_{i=1}^{2N} \frac{-1}{2N_{c_i} - 1} \sum_{j=1}^{2N} \mathbb{1}_{i \neq j} \cdot \mathbb{1}_{c_i = c_j} \cdot \log \frac{\exp(z_i \cdot z_j / \tau)}{\sum_{k=1}^{2N} \mathbb{1}_{i \neq k} \cdot \exp(z_i \cdot z_k / \tau)}, \quad (2)$$

where N_{c_i} denotes the number of z_i with label c_i in this minibatch, $\tau \in \mathbb{R}^+$ is a scalar temperature parameter, and $\mathbb{1}$ is the indicator function.

3.4 Entity extraction

In this section, we introduce the entity extraction module for processing text reports, into into medical entities for example, anatomy or observation, with their presence information. Anatomy refers to an anatomical body part that occurs in a radiology report, such as a “lung”. Observation refers to the word associated with visual features, physiological processes or diagnostic disease classifications, such as “effusion”, for each observation, the uncertainty level of its existence will be specified as present or absent. For each radiology text with more than one sentence, they will be converted into a sequence of entities and categories, *i.e.*, $t = \{e_1^1, s_1^1, [\text{SEP}], \dots, e_i^k, s_i^k, [\text{SEP}], \dots\}$, where e_i^k is the k -th extracted entity for i -th sentence, s_i^k is the category of e_i^k . The [SEP] token separates the entities. After extracting all entities from the reports, we select the top Q most commonly appearing observation entities from the entire reports corpus, denoted as an entity set $\mathcal{Q} = \{q_1, q_2, \dots, q_Q\}$, and get a label indicating the existence of the entity from the uncertainty level. For entities that are not mentioned in the report, we set their label as “absent” by default. We make three attempts on this goal.

First, we employed heuristic rules using the Unified Medical Language System (UMLS). Specifically, for each sentence in the radiology report, we were able to extract a sequence of entities (entity, concept, CUI, TUI) with the Python spacy package. The pseudo-code is provided in Supplementary Fig. 12. To determine the presence of an entity, we first filter the entity list for each sentence based on TUI, retaining only the entities with TUI in (T033: Finding, and T047: Disease or Syndrome). Next, we match these entities with our entity set, except for ‘normal’. Furthermore, we

adopted a straightforward heuristic rule: if the sentence contains the words 'no', 'none', or 'normal', the label is set to absent; otherwise, the label is set to 1 present. For entities that are not mentioned in the report, we assigned a label of absent. If all entities are absent, we set the label of 'normal' to present.

Second, we utilized the off-the-shelf RadGraph, for identifying radiology-specific entities and asserting their presence and anatomical relations from clinical text. RadGraph was trained on 500 radiology reports from the MIMIC-CXR dataset annotated by board-certified radiologists. With RadGraph, each radiology text was directly converted into a sequence of entities and categories. Each entity e_i^k will be classified into one of the following categories, defined as s_i^k : Anatomy (ANAT), Observation: Definitely Present (OBS-DP), Observation: Uncertain (OBS-U), and Observation: Definitely Absent (OBS-DA). For entities that are not mentioned in the report, we set their label as "definitely absent" by default.

Third, we experiment with ChatGPT [?], a large language model that has demonstrated remarkable results in natural language processing. We input the radiology report as the content to ChatGPT and use the following prompt:

For the given report of a chest x-ray, determine if the patient has any of the following findings: finding_list = [pleural effusion, opacity, pneumothorax, edema, atelectasis, tube, consolidation, enlarged cardiomeastinum, tip, pneumonia, line, cardiomegaly, fracture, calcification, medical device, engorgement, nodule, wire, pacemaker, pleural thicken, marking, scar, hyperinflate, blunt, collapse, emphysema, aerate, mass, infiltration, obscure, deformity, hernia, drainage, distention, shift, lesion, hardware, dilation, aspiration]. The output should use the following template: label_list = [i if finding exists for finding in finding_list]. If no finding exists, output label_list = []

We then processed the output label_list to obtain the presence of an entity.

3.5 Knowledge-guided visual representation learning

This section describes the detail of knowledge-guided visual representation learning. In particular, we introduce individual components of our architecture, including image encoder (Φ_{image}), knowledge encoder ($\Phi_{\text{knowledge}}$), disease query network (Φ_{dqn}). Lastly, we will describe the training procedure.

Image encoder. Given an X-ray image scan $x_i \in \mathbb{R}^{H \times W \times 3}$, we compute the features with a visual backbone:

$$\mathbf{x}_i = \Phi_{\text{image}}(x_i) \in \mathbb{R}^{m_x \times d}, \quad (3)$$

where d refers to the feature dimension, and $m_x = h \times w$ with h, w denoting the size of the output feature map. In our case, if the standard ResNet-50 [22] is adopted as the visual backbone, we take the output from the 4th residual block. And if the standard ViT-16 is used, we simply use the features from the transform encoder output.

Knowledge encoder. Given a pre-processed text report t_i , we compute the features with the pre-trained knowledge encoder:

$$\mathbf{t}_i = \Phi_{\text{knowledge}}(t_i) \in \mathbb{R}^{m_t \times d}, \quad (4)$$

where d refers to the feature dimension, and m_t refers to the token number.

Disease query network. Given the pre-defined entity set \mathcal{Q} , we compute a set of query vectors with the pre-trained knowledge encoder, $\mathcal{Q} = \{q_1, q_2, \dots, q_Q\}$, where $q_i = \Phi_{\text{knowledge}}(q_i)$. At training time, we randomly pick the encoded visual features \mathbf{x}_i or text features \mathbf{t}_i to act as the key and value of the disease query network (Φ_{dqn}), corresponding to the "Random Select" module in Fig. 1c. As ideally, we would like the visual and textual embedding space to be used interchangeably.

$$\hat{s}_i = \Phi_{\text{dqn}}(\mathbf{x}_i, \mathbf{t}_i, \mathcal{Q}) \in \mathbb{R}^{Q \times d}. \quad (5)$$

Note that during inference, we only use the visual features as the input of DQN. The outputs from the DQN are further fed into an MLP for inferring the existence of the query entity.

Training. We randomly sample a minibatch of N input pairs from the training data, and optimise the contrastive loss:

$$\mathcal{L}_{\text{contrast}} = -\left(\log \frac{e^{\langle \hat{\mathbf{x}}_i, \hat{\mathbf{t}}_i \rangle / \tau}}{\sum_{k=1}^N e^{\langle \hat{\mathbf{x}}_i, \hat{\mathbf{t}}_k \rangle / \tau}} + \log \frac{e^{\langle \hat{\mathbf{t}}_i, \hat{\mathbf{x}}_i \rangle / \tau}}{\sum_{k=1}^N e^{\langle \hat{\mathbf{t}}_i, \hat{\mathbf{x}}_k \rangle / \tau}}\right). \quad (6)$$

$\mathcal{L}_{\text{contrast}}$ denotes an image-to-text and text-to-image contrastive loss for the i -th pair respectively, where $\hat{\mathbf{x}}_i$ denotes the mean pooling over visual feature \mathbf{x}_i , $\hat{\mathbf{t}}_i$ denotes the mean pooling over text feature \mathbf{t}_i , $\langle \cdot, \cdot \rangle$ represents the cosine similarity, τ represents a temperature parameter.

As aforementioned, for each sample, we can obtain the existence label of the entity set \mathcal{Q} with the entity extraction module. Then for existence prediction, we use binary cross-entropy with the existence label, denoted as \mathcal{L}_{dqn} . Finally, for each mini-batch, we simply sum up $\mathcal{L}_{\text{contrast}}$ and \mathcal{L}_{dqn} as the overall loss.

$$\mathcal{L}_{\text{KAD}} = \mathcal{L}_{\text{contrast}} + \mathcal{L}_{\text{dqn}} \quad (7)$$

4 Experiments

4.1 Domain-specific Knowledge

To incorporate the medical domain knowledge into the training procedure of our proposed Knowledge-enhanced Auto Diagnosis system, we leverage a well-established medical knowledge graph (UMLS) for pre-training, and investigate various ways for medical entities extraction from reports.

UMLS Knowledge Graph. We leverage the Unified Medical Language System (UMLS) [4, 17] to serve as the knowledge base for training our proposed architecture. In detail, UMLS contains medical concepts (entities) that are integrated from different lexicon resources, each entity has a Concept Unique Identifier (CUI) with corresponding definition and multiple synonymous names, and has been assigned one or occasionally multiple semantic types. The UMLS also provides relation information between medical entities in the form of triplets, normally represented as (head entity, relation, tail entity), for example, (adenoviral pneumonia, has finding site, lungs pair), as shown in Fig. 1a.

Entity Extraction. We explore three different ways, namely, heuristic rules, RadGraph, or ChatGPT, to preprocess the given X-ray reports, converting them from raw texts into medical entities and their presence, for example, sentence ‘‘There is no consolidation, effusion, or pneumothorax.’’ will be converted into {consolidation, absent, [SEP], effusion, absent, [SEP], pneumothorax, absent}. the extraction procedure will be detailed in the following sections.

4.2 Datasets

4.2.1 Dataset for pre-training

In our experiments, we conduct model pre-training on MIMIC-CXR [29], it is a publicly available dataset of chest radiographs with radiology text reports. The MIMIC-CXR dataset contains 377,110 images corresponding to 227,835 radiographic studies for 65,379 patients. Each radiographic study come with a free-text radiology report and corresponding chest X-ray images (in frontal or lateral views). The radiology report is a summarization written by radiologists regarding their findings, that consists of multiple sections: examination, indication, impression, findings, technique, and comparison. In practice, we only keep the findings and impressions sections in the reports.

4.2.2 Datasets for downstream evaluation

To evaluate the model, we conduct experiments on both zero-shot transfer and model fine-tuning. The details of the datasets and implementation details are described below.

PadChest [8]. PadChest has 160,868 chest X-ray images labeled with 174 different radiographic findings, 19 differential diagnoses, only 27% of the labels (totaling 39,053 examples) come from board-certified radiologists, and the rest are obtained by using a recurrent neural network with attention trained on the radiology reports. For evaluation purposes, we only test on samples annotated by board-certified radiologists, and report the zeros-shot transfer results.

ChestXray14 [53]. NIH ChestXray14 has 112,120 chest X-ray images with disease labels from 30,805 unique patients. The disease labels are acquired by mining the associated radiological reports with natural language processing tools. In total, there are 14 disease labels: Atelectasis, Cardiomegaly, Effusion, Infiltration, Mass, Nodule, Pneumonia, Pneumothorax, Consolidation, Edema, Emphysema, Fibrosis, Pleural Thickening and Hernia. In this paper, all models are tasked to predict a binary label for each of these 14 disease labels for each X-ray image from the dataset, resembling a multi-label classification problem. We strictly follow the official patient-wise data split from original ChestXray14 release, and use the images from 10% subjects in the training set to form a validation set.

CheXpert [26]. CheXpert has 224,316 chest X-ray images collected from 65,240 patients. The official validation set contains 200 chest radiographic studies that are manually annotated by 3 board-certified radiologists, and the official test set contains 500 chest radiographic studies annotated by a consensus of 5 board-certified radiologists [45]. We use the validation dataset for picking the thresholds of predictions. We follow the original paper, and focus on the evaluation of 5 observations on the official test set (the competition tasks): Atelectasis, Cardiomegaly, Consolidation, Edema and Pleural Effusion.

ChestX-Det10 [35]. ChestX-Det10 is a subset of NIH ChestXray14, which is consisting of 3543 chest X-ray images with box-level annotations provided by 3 board-certified radiologists of 10 diseases/abnormalities, including Atelectasis, Calcification, Consolidation, Effusion, Emphysema, Fibrosis, Fracture, Mass, Nodule and Pneumothorax. In this paper, we follow the official data split and report the zero-shot grounding results on the test set.

4.3 Baselines

In general, existing state-of-the-art models can be cast into two categories based on the modalities involved at the pre-training stage: medical image-text pre-training approaches, which enable both zero-shot transfer and fine-tuning, medical image pre-training approaches, that only support fine-tuning evaluation. Note that, all above baselines are implemented using the same backbone architecture as our KAD, *i.e.*, a ResNet-50 [22] architecture as the basic image encoder module. Such an implementation decision rules out the effect of network architectures on final performance and advocates fairness in experimental comparisons.

4.3.1 Medical image-text pre-training methods

In this section, we introduced the compared state-of-the-art medical image-text pre-train methods, namely, ConVIRT [61], GLoRIA [23], BioViL [5] and CheXzero [49]. Since ConVIRT and GLoRIA are pre-trained on an in-house dataset, we re-train their models on the MIMIC-CXR [29] dataset for fair comparison. For BioViL and CheXzero, we use the officially released models by the authors.

ConVIRT [61] jointly trains the vision and text encoders with the paired medical images and reports via bidirectional contrastive learning.

GLoRIA [23] models the interactions between medical images and reports via both global and regional contrastive learning.

BioViL [5] leverages a pre-trained radiology-specific text encoder for contrastive learning using paired image-text radiology data.

CheXzero [49] fine-tunes the pre-trained CLIP model [44] on the X-ray and reports with contrastive learning using image-text pairs.

MedKLIP [55] leverages medical-specific knowledge descriptions to enhance visual-language pre-training using paired image-text data.

4.3.2 Medical image pre-training methods

In this section, we introduced the compared medical image pre-training approaches, namely, Model Genesis [64], Comparing to Learn (C2L) [62] and ImageNet Pre-training [15]. For Model Genesis

and C2L, we re-train their models on the MIMIC-CXR [29] dataset with their official codes for a fair comparison.

Model Genesis [64] refers to the self-supervised visual representation learning approach, that considers restoring the original image from artificial distortion, including local shuffling, non-linear transformation, in- and out-painting.

Comparing to Learn (C2L) [62] refers to the self-supervised visual representation learning approach, that generates positive and negative pairs through both image and feature level mix-up for contrastive learning.

ImageNet Pre-training [15] refers to a representative method that is pre-trained on a large-scale dataset of natural images, with supervised learning.

4.4 Implementation details

Data pre-processing. At the visual-language pre-training stage, we resize each chest X-ray image to 224×224 , and normalise it with sample mean and standard deviation computed from the whole training dataset. Random resize crop, random horizontal flip, random rotation (-10 to 10 degrees) and random grayscale (brightness, sharpness and contrast) are applied as data augmentation. For radiology reports, we first apply named entity recognition and linking tool, ScispaCy [42] to pre-process the texts, *i.e.*, extract the entities from reports and ground them in the UMLS knowledge base for entity disambiguation. Then, we use RadGraph [27] to obtain the corresponding semantic types for each entity with uncertainty levels. The entities with corresponding semantic types and uncertainty levels are concatenated as input, *e.g.*, {pleural effusion, observation definitely present, [SEP], lung, anatomy, [SEP],...}, and the maximal sequence length is 256. At the fine-tuning stage, we apply the same set of strategies for pre-processing, as in pre-training for all four target domain datasets.

Model pre-training. The overall framework generally follows a two-stage training pipeline. For Stage1, we initialize the knowledge encoder from the English version PubMedBERT [21], and finetune it for 100K training steps. In each mini-batch, 64 concept-definition pairs and 64 concept-relation-concept triplets are used for training. The maximal sequence length is 256 since the definition could be long. We use AdamW [36] as the optimizer with $lr = 1 \times 10^{-4}$ and $lr_{\text{warm up}} = 1 \times 10^{-5}$. For Stage2, the image encoder is the first four layers of ResNet50, the DQN is composed of a series of standard Transformer decoders [50]. We use AdamW optimizer with $lr = 1 \times 10^{-4}$ and $lr_{\text{warm up}} = 1 \times 10^{-5}$. We train on an A100 with batch size 64 for 50 epochs. The first 5 epochs are set for warming up.

Zero-shot transfer. To evaluate the zero-shot performance of the model on the multi-label classification task, DQN takes the disease name list as query input, and image features as key and value, and output the likelihood of the disease being present in the considered chest X-ray image. The average cross-attention between the disease and the visual features are used for grounding. For other medical image-text pre-training baselines, we use the prompt defined in BioVIL [5], for example, representing presence/absence of pneumonia: “Findings suggesting pneumonia” and “No evidence of pneumonia”.

Model fine-tuning. At this stage, we fine-tune all models using AdamW optimizer with $lr = 1 \times 10^{-4}$ for all datasets. The model is trained with the same learning rate, and decay strategy as that used in the pre-training stage, and are trained with a batch size of 64.

4.5 Evaluation details

Statistical analysis. In our evaluation, AUC stands for “Area under the ROC Curve”, MCC stands for “Matthews Correlation Coefficient”, F1 stands for “F1 score” and ACC stands for “Accuracy”. We collect AUC results directly using model’s prediction, while to obtain the MCC, we first run inference on the test set to get the probability values for the different classes on each chest X-ray image. The probabilities are then transformed into positive/negative predictions with thresholds found by optimizing MCC over the validation dataset. Then, the condition-based MCC scores are calculated using these predictions. We similarly compute the F1 score and ACC, but using the same

thresholds as used for computing the MCC. For zero-shot grounding, we use Pointing Game [60] for evaluation purpose. In specific, we extract the region with maximum response in the output heat map, and if the region hit the ground-truth mask, it is considered a positive prediction, otherwise negative. Finally, accuracy can be calculated as the pointing game score.

Confidence intervals. We use the non-parametric bootstrap to generate confidence intervals: random samples of size n (equal to the size of the original dataset) are repeatedly sampled 1,000 times from the original dataset with replacement. We then estimate the AUC, MCC, F1 and ACC metrics using each bootstrap sample. The predicted probabilities are then transformed into positive/negative predictions using the thresholds found by optimizing MCC over the validation dataset. We derive confidence intervals from the relative frequency distribution of the estimates over the re-samples, using the interval between the $100 \times (\alpha/2)$ and $100 \times (1 - \alpha/2)$ percentiles; we pick $\alpha = 0.05$.

5 Results

The goal of our proposed Knowledge-enhanced Auto Diagnosis (KAD) is to improve vision-language pre-training and facilitate the auto-diagnosis for chest X-ray images, by leveraging domain knowledge, for example, in pre-defined knowledge graph (Unified Medical Language System, UMLS) [4], or off-the-shelf named entity recognition toolbox (RadGraph) [27]. In this section, all baselines are pre-trained on the MIMIC-CXR [29] dataset, and directly evaluated on four well-established multi-center datasets, *i.e.*, zero-shot inference, including PadChest [8], NIH ChestX-ray [53], CheXpert [26], and ChestX-Det10 [35]. In all cases, the model makes inferences by predicting whether the queried disease exists in the input image.

Note that, at the core of our study, is to develop a pre-training procedure for incorporating medical domain knowledge, *e.g.*, UMLS, RadGraph, such design naturally equips KAD with additional information than existing self-supervised approaches. However, from a practical perspective, KAD training only exploits off-the-shelf tools, thus is equally scalable to large datasets as self-supervised learning approaches do, while demonstrating significantly more superior performance on identifying diseases not encountered at training time, and handling long-tail recognition problem. We conduct extensive ablation studies to analyze the contribution of certain model components, and the impact of image resolution and visual backbone.

5.1 PadChest

We evaluate KAD on the diagnosis task in PadChest dataset, where the images are labeled with 174 different radiographic findings and 19 differential diagnoses. The fundamental challenge of PadChest dataset lies in the long-tailed class distribution, as illustrated in Supplementary Fig. 7, where only 21 classes have more than 1000 samples, and only 16 classes are seen during pre-training. Here, we denote the diseases that are seen by Disease Query Network (DQN) at the model training stage as seen diseases, and the others as unseen diseases. As shown in Fig. 2 b, KAD outperforms existing SOTA models on most unseen radiographic findings, and the model achieves an AUC of at least 0.900 on 31 classes and at least 0.700 on 111 classes out of 177 **unseen** classes in the PadChest test dataset ($n = 39, 053$) Supplementary Fig. 8, 9, 10 and 11 includes results on all 193 radiographic findings and diagnoses. As shown in Fig. 2 a, while comparing the performance with **fully-supervised** model, we observe that KAD significantly outperforms CheXNet on five out of the seven pathologies diagnosis, with AUC of 0.809 (95% confidence interval (CI) 0.796, 0.822) for atelectasis, 0.916 (95% CI 0.913, 0.919) for cardiomegaly, 0.910 (95% CI 0.896, 0.924) for consolidation, 0.966 (95% CI 0.958, 0.974) for edema and 0.835 (95% CI 0.829, 0.842) for pneumonia; additionally, KAD demonstrates superior performance than other existing self-supervised visual-language models using image-text pairs, for example, AUC 11% higher on pneumothorax than CheXzero [49].

5.2 ChestXray14

Fig. 3 and Supplementary Table 3 and 4 present results of KAD and other approaches on NIH ChestXray14 dataset, where the images are labeled with 14 different diseases, including only one unseen class “fibrosis”, not appearing in any of the reports used for training. We conduct extensive experiments on both zero-shot and fine-tuning settings, in the latter case, we verify the model’s performance by varying the percentage of images for fine-tuning. As shown in Supplementary

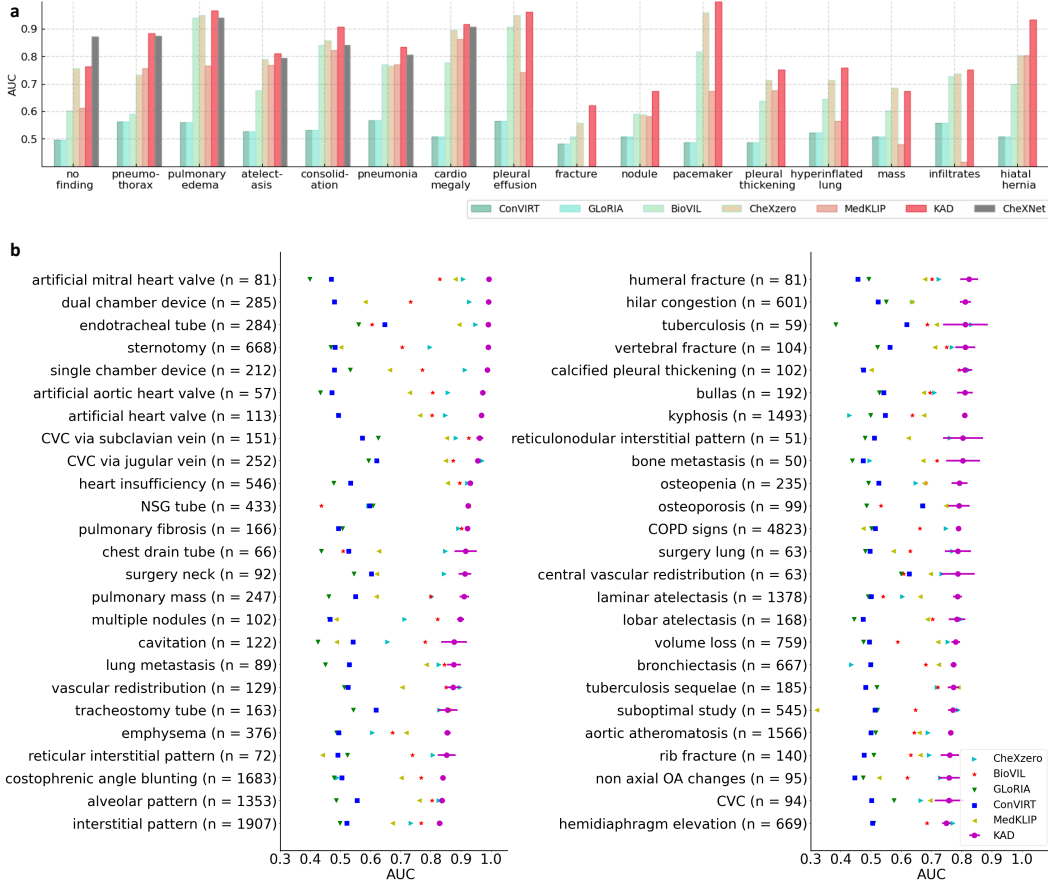


Figure 2: Comparison of KAD with SOTA medical image-text pre-training models under **zero-shot** setting on radiographic findings or diagnoses in the **PadChest** dataset. We evaluate model on the human-annotated subset of the PadChest dataset ($n = 39,053$ chest X-rays) and mean AUC and 95% CI of KAD are shown for each radiographic finding or diagnoses ($n > 50$). **a**, Results of seen classes. Note that CheXNet is a **supervised** model trained on the **PadChest** dataset. **b**, Results of unseen classes. KAD achieves an AUC of at least 0.900 on 31 classes and at least 0.700 on 111 classes out of 177 **unseen** classes in the PadChest test dataset. Top 50 classes where ($n > 50$) in the test dataset ($n = 39,053$) are shown in the figure.

Table 3, KAD achieves the highest performance over all existing self-supervised visual-language models trained with image-text pairs, for instance, it gives an average AUC of 0.786 (95% CI 0.770, 0.808). For 13 of the 14 pathologies, KAD gets significantly higher AUC than the best-performing baseline. Additionally, in the fine-tuning scenario shown in Supplementary Table 4, KAD also demonstrates substantial improvements on all evaluation metrics over the existing approaches. As we can see, KAD consistently maintains large advantages over other methods under different labeled conditions, and exhibits the largest performance improvements with respect to these baselines when only 1% data is used for training, for example, KAD surpasses ConVIRT by about 13.8%, and the widely adopted ImageNet-based pre-training by about 15.2% on average, with largest improvements on hernia ($> 29\%$) and edema ($> 10\%$), especially under limited supervision.

5.3 CheXpert

Fig. 4 and Supplementary Table 5 present experimental results from KAD and other image-text pre-training models, the performance is compared to three human radiologists on CheXpert test set. The results show that KAD consistently outperforms existing approaches on the average evaluation scores, demonstrating strong generalisation ability. When compared with the mean performance of three radiologists, it is notable that KAD achieves statistically higher mean Matthews Correlation

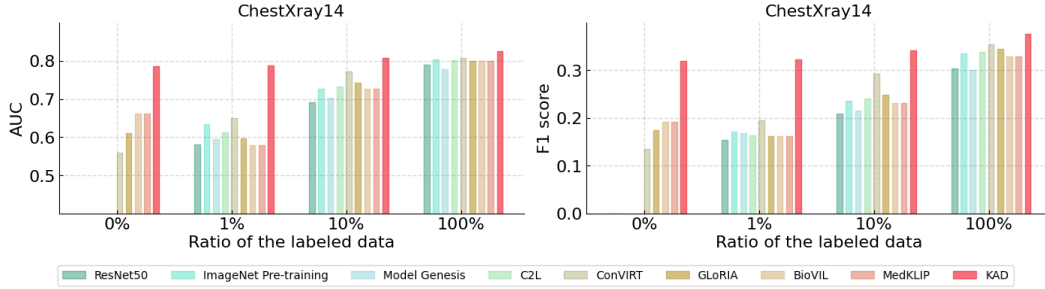


Figure 3: Comparison of proposed KAD with SOTA self-supervised baseline models and medical image-text pre-training models on **ChestXray14** with different ratio of labeled data used for **fine-tuning**. AUC, F1 score are reported, and the metrics refer to the macro average on all the diseases. Note that for fairness, all baselines use the same backbone as the basic image encoder (that is, ResNet50). The percentages refer to the percentage of labels used in the training data.

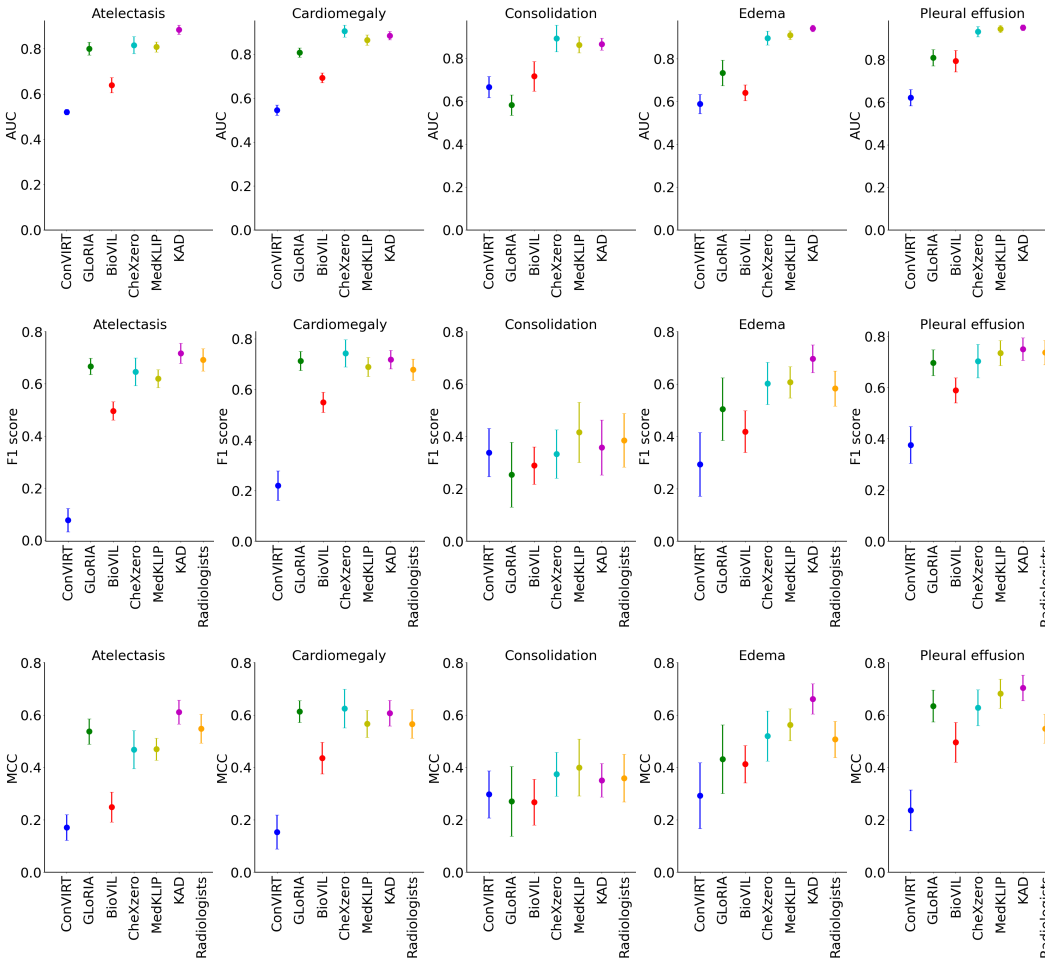


Figure 4: Comparisons of proposed KAD with SOTA medical image-text pre-training models and three board-certified radiologists on five competition pathologies in **CheXpert** dataset. Note that, all models are directly evaluated on CheXpert dataset under **zero-shot** setting. The AUC, F1 scores and MCC of five pathologies are shown in the plots, where the average and 95% CI are shown. Details in Supplementary Table 5.

Coefficient (MCC) metric on majority of the competition pathologies. In particular, on atelectasis (KAD 0.613 (95% CI 0.567, 0.659) vs. Radiologists 0.548), edema (KAD 0.666 (95% CI 0.608,

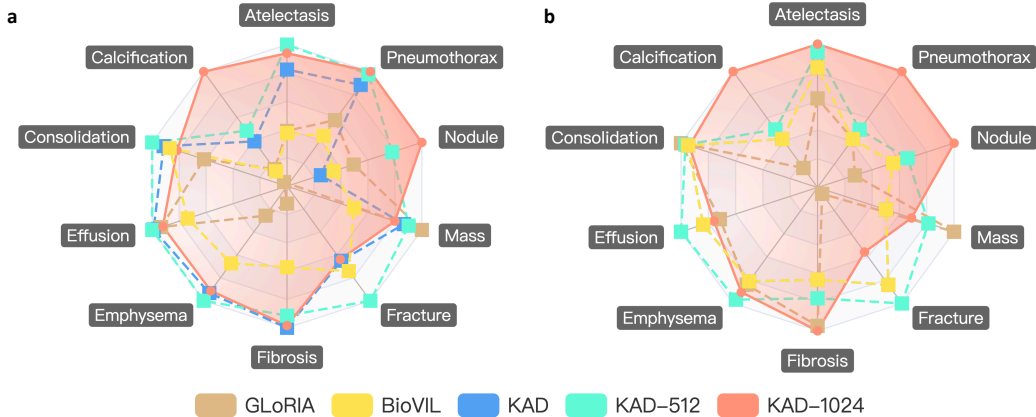


Figure 5: Comparisons of proposed KAD with SOTA medical image-text pre-training models on ChestX-Det10 dataset. AUC scores are shown for the zero-shot classification task in (a), and Pointing game scores are shown for the zero-shot grounding task in (b). We use the best results as the maximum value for each category in the radar chart, and 0.5 as the minimal value for (a), 0 as the minimal value for (b). Details in Supplementary Table 6.

0.724) vs. Radiologists 0.507) and pleural effusion (KAD 0.702 (95% CI 0.653, 0.751) vs. Radiologists 0.548). On consolidation (Radiologists 0.359 (95% CI 0.262, 0.444) vs. KAD 0.357), our model is slightly worse, but not statistically significantly. On the F1 metric, there is no statistically significant difference between the mean performance from KAD 0.647 (95% CI 0.591, 0.702) and that of the radiologists 0.619 (95% CI 0.585, 0.642), with only exception on edema, where KAD performs significantly better (KAD 0.701 (95% CI 0.647, 0.754) vs. Radiologists 0.583).

5.4 ChestX-Det10

Fig. 5 shows the results for zero-shot diagnosis and grounding on the ChestX-Det10 test set. Our proposed model outperforms existing methods on majority and mean values. Specifically, KAD obtains significant improvements over GLoRIA [23] on the difficult categories, *i.e.*, calcification (> 7%) and fracture (> 18%). Additionally, it is worth noting that the ability to localize disease is significantly improved with the image resolution increasing, especially for some diseases with small bounding boxes, KAD-1024 shows not only higher accuracy but also better precision.

5.5 Ablation study

We conduct a thorough ablation study of KAD, systematically varying one variable at a time. By default, our model comprises the image encoder, knowledge encoder, random select module, and disease query network, and incorporates RadGraph for entity extraction. Table 1 shows the quantitative results, indicating that the proposed modules are effective for addressing the limitations of the previous approach: knowledge deficit, report complexity, and limited transferability. We also perform experiments to analyze the impact of image resolution and visual backbone (Table 2).

Knowledge encoder. “KAD w/o Stage1” refers to using PubMedBERT [21] as text encoder without finetuning on medical knowledge graph. We show the similarity map between features of different disease names encoded by PubMedBERT and the pre-trained text encoder in Supplementary Fig. ??, our knowledge-enhanced text encoder clearly distinguishes the features of different diseases, while PubMedBERT encodes them almost identically.

Cross-modal contrastive learning without entity extraction. “KAD w/o entity extraction” refers to not using entity extraction module in cross-modal contrastive loss (Eq. 6), *i.e.*, simply align the raw reports and images. As shown in the table, with the entity extraction module, the classification results can be improved from 0.772 to 0.786 on AUC in ChestX-ray14 dataset, and 0.897 to 0.906 on AUC in CheXpert dataset. These results demonstrate the benefits of standardized reports for training.

Methods for entity extraction. “w/ UMLS” refers to employing only heuristic rules for entity extraction. “w/ RadGraph”, “w/ ChatGPT” refers to utilizing RadGraph and or ChatGPT, respectively. Based on the results, it can be observed that although heuristic rules slightly under-perform in comparison, it is already very competitive, and RadGraph and ChatGPT perform equally well. It should be noted that different approaches for extracting entities yielded similar results, indicating that the specific method used for entity extraction was not the primary factor affecting performance in KAD. The critical component is our proposed DQN architecture.

Random select module. “KAD w/o random select” refers to removing the random select module, *i.e.*, only use the image features as the key and value of the disease query network. The results in Table 1 verify that the random select module help to align image features and text features in the textual embedding space, thus improving the zero-shot performance.

Disease query network. “KAD w/o DQN” refers to only training with contrastive learning in Stage2, *i.e.*, similar design as the existing image-text pre-training models, which incurs the most significant performance degradation, showing the necessity of DQN for better generalization on disease diagnosis or radiology findings.

Image encoders and Image resolutions. As shown, performance with ResNet and ViT are comparable, demonstrating that the proposed knowledge-enhanced representation learning is robust to the selection of image encoder. And the results of KAD-512 and KAD-1024 show that the ability to diagnose is not noticeably improved with the image resolution increasing, compared to image localization (Fig. 5).

Table 1: Ablation study of KAD under **zero-shot** setting by removing or replacing individual modules. KAD w/o Stage1 uses PubMedBERT as the text encoder. KAD w/o random select uses only image features as key or value when training DQN. KAD w/o DQN only trains the cross-modal contrastive learning part and test like previous image-text pre-training models. We also perform ablation on the entity extraction tool. w/ heuristic rule uses UMLS based on heuristic rule for entity extraction instead of RadGraph. w/ ChatGPT uses the large language model for entity extraction. w/ RadGraph utilizes the reports information extraction toolbox, RadGraph for entity extraction. Note that for fairness, all baselines use the same backbone as the basic image encoder (that is, ResNet50). Numbers within parentheses indicate 95% CI. The best results are bold.

Methods	ChestXray14				CheXpert			
	AUC	MCC	F1	ACC	AUC	MCC	F1	ACC
Ablation on proposed modules.								
KAD w/o Stage1	0.752	0.228	0.274	0.748	0.894	0.546	0.620	0.858
KAD w/o random select	0.751	0.242	0.290	0.780	0.878	0.571	0.671	0.812
KAD w/o DQN	0.672	0.144	0.109	0.747	0.822	0.419	0.508	0.806
Ablation on entity extraction module								
w/ UMLS	0.773	0.268	0.308	0.833	0.904	0.562	0.635	0.867
w/ ChatGPT	0.784	0.284	0.336	0.845	0.887	0.573	0.622	0.888
w/ RadGraph (KAD)	0.789	0.280	0.323	0.816	0.905	0.589	0.647	0.875

Table 2: Ablation study of KAD with different image encoders and different image resolutions. AUC, MCC, F1 and ACC scores are reported, and the metrics all refer to the macro average on all the diseases. Numbers within parentheses indicate 95% CI. The best results are bold.

Image Encoder	Size	ChestXray14				CheXpert			
		AUC	MCC	F1	ACC	AUC	MCC	F1	ACC
ResNet-50 [22]	224	0.789	0.280	0.323	0.816	0.905	0.589	0.647	0.875
ViT-16 [18]	224	0.785	0.276	0.321	0.807	0.907	0.575	0.647	0.884
ResNet-50 [22]	512	0.788	0.278	0.321	0.817	0.908	0.595	0.656	0.874
ResNet-50 [22]	1024	0.802	0.306	0.347	0.828	0.902	0.556	0.607	0.836

6 Discussion

The purpose of this work was to develop a foundation model for chest X-rays by exploiting the existing knowledge prior in medical domain. Here, we provide a discussion to analyze the performance of KAD from different perspectives.

KAD achieves comparable results with expert radiologists. While comparing KAD to human expert radiologists on CheXpert, the results in Fig. 4 indicate that the model can keep up or even **surpass** the performance of experienced clinicians in some diagnostic tasks, *i.e.*, KAD achieves statistically higher MCC on the average of five pathologies, over mean performance of three radiologists, demonstrating the effectiveness of knowledge-enhanced pre-training. As a result, the proposed KAD model can serve as a reference when disagreement occurs among physicians.

KAD achieves comparable results to supervised models. As shown in Fig. 2a, the performance of KAD is comparable to, and sometimes exceeds, fully supervised methods on PadChest, for example, KAD brings a 6.8% performance gain on “consolidation”. Note that KAD achieves such results without seeing any training images from PadChest, which is collected in a different country from the training dataset MIMIC-CXR. Additionally, as shown in Fig. 2b, the application of a fully supervised model is limited to a closed set of categories, while KAD allows the query input to be arbitrary pathologies, identifying radiological findings with high accuracy on PadChest, demonstrating strong generalization ability and robustness to various clinical diagnosis categories.

KAD enables superior results on zero-shot diagnosis. By establishing connections between images and texts, vision-language models are able to turn visual classification into zero-shot inference beyond limited set of pathologies. In contrast to existing approaches that directly match raw reports with image scans, we leverage domain knowledge from well-structured knowledge graph (UMLS), and pre-process the reports by extracting medical entities. As in the report, the same medical concept can appear in various forms, for example, nonstandard names, abbreviations, and misspellings in the reports, which may lead to noisy supervision. While our proposed knowledge-enhanced mechanism enables the establishment of relations between different radiological concepts, thus enables generalization to unseen classes, as suggested by the results on PadChest (Fig. 2), KAD enables to identify and diagnose radiological findings with high accuracy on 177 unseen classes.

KAD enables data-efficient transfer across various tasks. When manual annotations for target downstream datasets are available, KAD consistently outperforms the existing visual-language models under different finetuning settings, *i.e.*, using a variable number of data for finetuning, as shown in Fig. 3. Note that, in the following classes, including cardiomegaly, effusion, pneumonia, pneumothorax, and hernia, KAD required only 1% labeled data to achieve better results than others under 100% label ratio, showing potential of KAD in data-efficient transfer learning. Such phenomenon indicates that KAD can fully inherit the benefits from pre-training, *i.e.*, leveraging both the DQN module and the pre-trained text encoder.

KAD provides grounded heatmap for making clinical decisions. In addition to auto-diagnosis, explainability is equally critical in AI-assisted applications, as it may help clinicians to discover and understand the evidences that AI algorithm bases its predictions on, potentially presenting transparency and enabling better collaboration in the clinical setting. Here, we qualitatively analyze KAD by averaging the cross-attention map in each transformer layer in DQN, and visualizing the results of KAD with different resolutions in Fig. 6. It can be observed that the model is indeed pooling information from regions that well match radiologists’ diagnoses on different pathologies, *i.e.* red boxes labeled by board-certified radiologists. Quantitatively, we evaluate KAD on ChestX-Det10 and present the pointing game results in Fig. 5, which further confirms the provided explanations.

Limitation and future work. Despite the ability of KAD on zero-shot and data-efficient transfer, there remains a few limitations: *First*, the pre-trained model still requires a small validation set for hyper-parameter tuning, *e.g.*, to determine the probability threshold of a specific disease. *Second*, some pathologies, may not have any relation with other diseases in the knowledge base, and never be mentioned in the reports, for example, pectum carinatum, our method is not expected to predict that pathology with high accuracy during zero-shot evaluation for this case. *Third*, diagnosis of KAD is limited to classification and coarse grounding, and not able to provide accurate segmentation. As

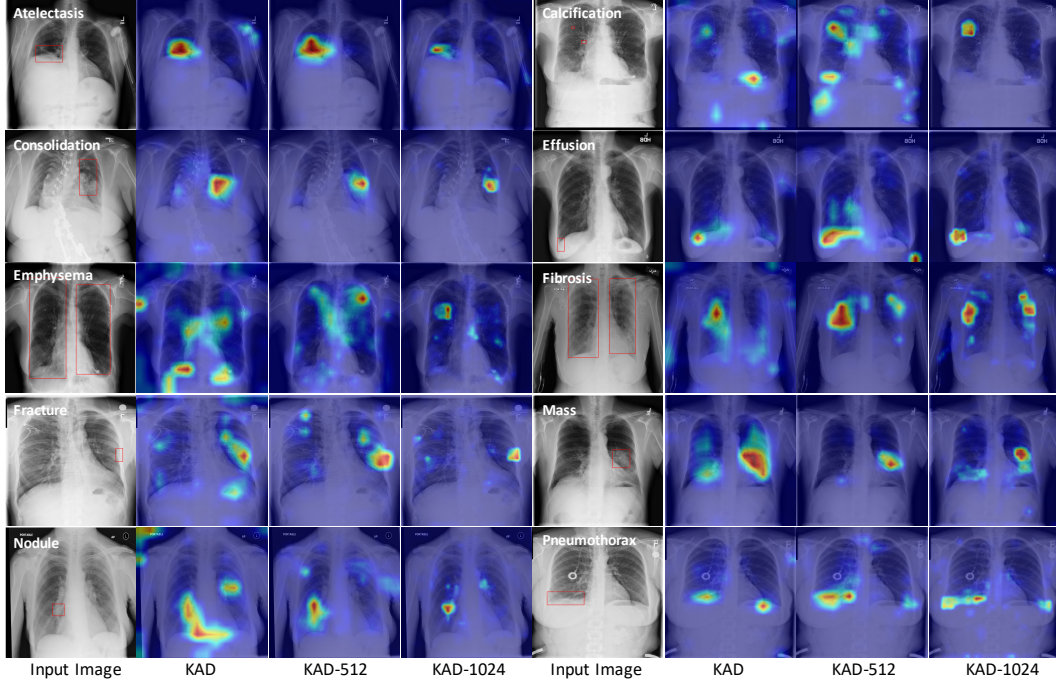


Figure 6: **Zero-shot** visualization of randomly chosen samples from ChestX-Det10, we present both the original image (left) and attention maps generated from KAD, KAD-512 and KAD-1024. In the original images, red boxes denote lesion areas annotated by radiologists. In the attention maps, the red to blue spectrum are plot on the original image with red representing high attention regions and blue representing low attention.

future work, we would extend the knowledge-enhanced training to more diverse medical tasks, where structured or unstructured can be acquired with negligible cost.

Clinical impact analysis. In summary, our proposed KAD leverages paired X-ray images and the clinical reports for vision-language pre-training, incorporating medical knowledge from a well-established knowledge graph. As a result, the model has demonstrated significant performance improvement and robustness over existing approaches in auto-diagnosis for chest X-ray images. Our findings in this paper, provide inspirations for resolving a few concerns, that potentially hinder the feasibility of developing foundation models for more general medical diagnosis applications. Firstly, laborious data curation. large-scale data collection incurs time-consuming procedure, especially on unifying the data format and terminology in clinical reports. KAD adopts an off-the-shelf domain-specific entity extraction module that automatically simplifies the raw reports into a set of meaningful medical terminologies. Secondly, limited and exorbitant expert knowledge, the analysis of medical image data heavily relies on domain-specific expert knowledge, KAD first learns a neural representation of the knowledge graph, that captures the implicit relation between medical entities in the textual embedding space, benefits the model’s generalization on long-tailed target tasks. Lastly, model interpretation, KAD diagnoses with an attention map output enables the clinicians to understand the model’s decision-making procedure and thus encourage the trustiness.

7 Conclusion

In conclusion, we propose a knowledge-enhanced vision-language pre-training model, termed as KAD, for the auto-diagnosis of chest X-ray images. The training involves two stages, first, we train a knowledge encoder to learn a neural representation of an existing medical knowledge graph, second, we extract the clinical entities and relations from the radiology reports by the off-the-shelf named entity recognition toolbox, and employ the pre-trained text encoder to perform image-text contrastive learning with paired chest X-rays and extracted entities, and optimize a Disease Query Network for classification. In experiments, we evaluate our method on four different datasets under various settings, showing strong zero-shot performance compared with state-of-the-art self-supervised and supervised methods, even exceeding the average for expert radiologists on multiple pathologies.

References

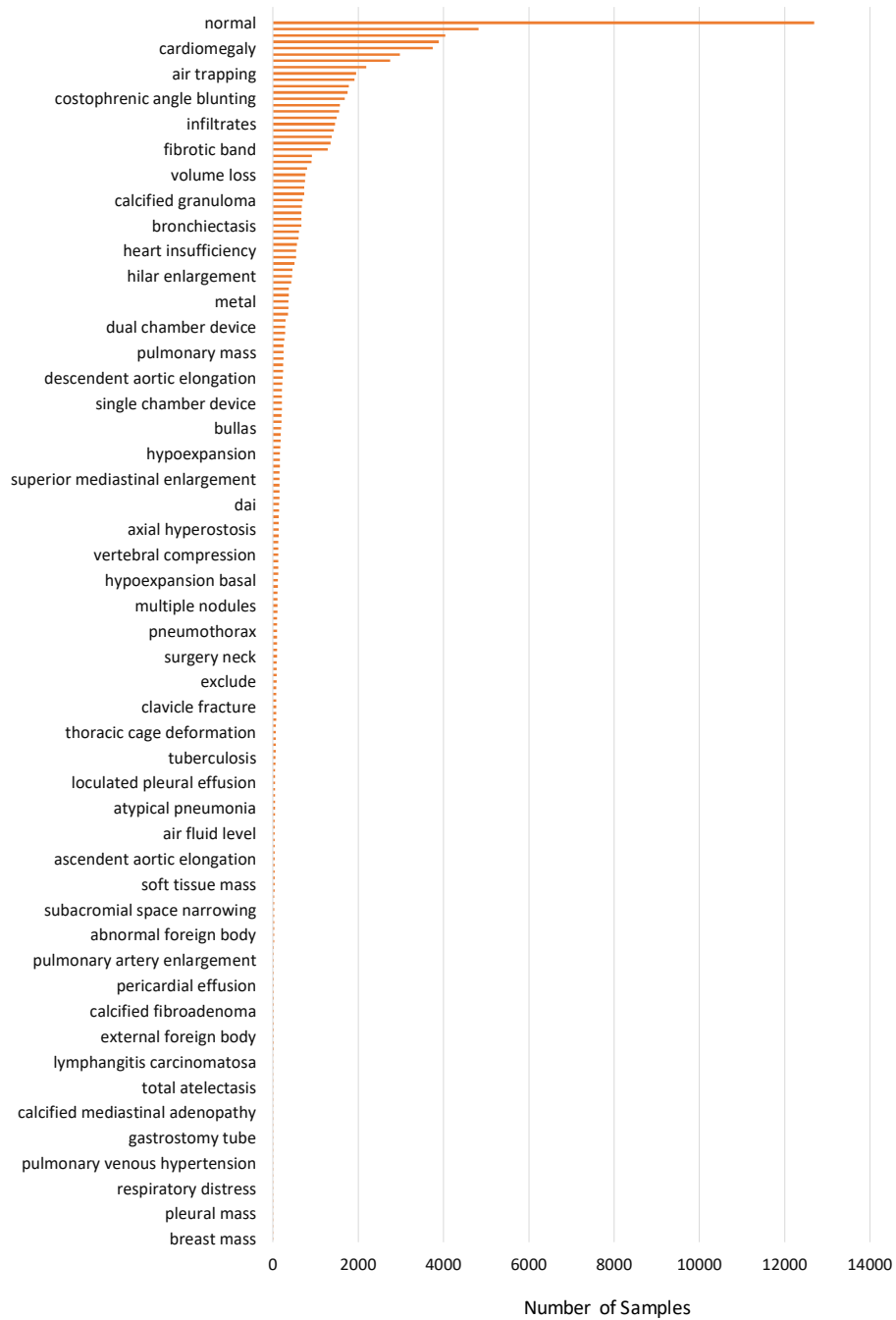
- [1] Jean-Baptiste Alayrac, Jeff Donahue, Pauline Luc, Antoine Miech, Iain Barr, Yana Hasson, Karel Lenc, Arthur Mensch, Katie Millican, Malcolm Reynolds, et al. Flamingo: a visual language model for few-shot learning. *arXiv preprint arXiv:2204.14198*, 2022. [1](#)
- [2] Alan R Aronson and François-Michel Lang. An overview of metamap: historical perspective and recent advances. *Journal of the American Medical Informatics Association*, 17(3):229–236, 2010. [3](#)
- [3] Federico Bianchi, Giuseppe Attanasio, Raphael Pisoni, Silvia Terragni, Gabriele Sarti, and Sri Lakshmi. Contrastive language-image pre-training for the italian language. *arXiv preprint arXiv:2108.08688*, 2021. [3](#)
- [4] Olivier Bodenreider. The unified medical language system (umls): integrating biomedical terminology. *Nucleic acids research*, 32(suppl_1):D267–D270, 2004. [3](#), [4](#), [6](#), [9](#)
- [5] Benedikt Boecking, Naoto Usuyama, Shruthi Bannur, Daniel C Castro, Anton Schwaighofer, Stephanie Hyland, Maria Wetscherek, Tristan Naumann, Aditya Nori, Javier Alvarez-Valle, et al. Making the most of text semantics to improve biomedical vision–language processing. In *European conference on computer vision*, pages 1–21, 2022. Official Implementation: <https://github.com/microsoft/hi-ml/tree/main/hi-ml-multimodal>. [3](#), [7](#), [8](#)
- [6] Rishi Bommasani, Drew A Hudson, Ehsan Adeli, Russ Altman, Simran Arora, Sydney von Arx, Michael S Bernstein, Jeannette Bohg, Antoine Bosselut, Emma Brunskill, et al. On the opportunities and risks of foundation models. *arXiv preprint arXiv:2108.07258*, 2021. [1](#)
- [7] Tom Brown, Benjamin Mann, Nick Ryder, Melanie Subbiah, Jared D Kaplan, Prafulla Dhariwal, Arvind Neelakantan, Pranav Shyam, Girish Sastry, Amanda Askell, et al. Language models are few-shot learners. *Advances in neural information processing systems*, 33:1877–1901, 2020. [1](#)
- [8] Aurelia Bustos, Antonio Pertusa, Jose-Maria Salinas, and Maria de la Iglesia-Vayá. Padchest: A large chest x-ray image dataset with multi-label annotated reports. *Medical image analysis*, 66:101797, 2020. [2](#), [6](#), [9](#)
- [9] Geeticka Chauhan, Ruizhi Liao, William Wells, Jacob Andreas, Xin Wang, Seth Berkowitz, Steven Horng, Peter Szolovits, and Polina Golland. Joint modeling of chest radiographs and radiology reports for pulmonary edema assessment. In *International Conference on Medical Image Computing and Computer-Assisted Intervention*, pages 529–539. Springer, 2020. [3](#)
- [10] Sihong Chen, Jing Qin, Xing Ji, Baiying Lei, Tianfu Wang, Dong Ni, and Jie-Zhi Cheng. Automatic scoring of multiple semantic attributes with multi-task feature leverage: a study on pulmonary nodules in ct images. *IEEE transactions on medical imaging*, 36(3):802–814, 2016. [3](#)
- [11] Yen-Chun Chen, Linjie Li, Licheng Yu, Ahmed El Kholy, Faisal Ahmed, Zhe Gan, Yu Cheng, and Jingjing Liu. Uniter: Universal image-text representation learning. In *European conference on computer vision*, pages 104–120. Springer, 2020. [3](#)
- [12] Zhihong Chen, Guanbin Li, and Xiang Wan. Align, reason and learn: Enhancing medical vision-and-language pre-training with knowledge. In *Proceedings of the 30th ACM International Conference on Multimedia*, pages 5152–5161, 2022. [1](#)
- [13] Hui Cui, Yiyue Xu, Wanlong Li, Linlin Wang, and Henry Duh. Collaborative learning of cross-channel clinical attention for radiotherapy-related esophageal fistula prediction from ct. In *International Conference on Medical Image Computing and Computer-Assisted Intervention*, pages 212–220. Springer, 2020. [3](#)
- [14] Robert Dale. Gpt-3: What’s it good for? *Natural Language Engineering*, 27(1):113–118, 2021. [1](#)
- [15] Jia Deng, Wei Dong, Richard Socher, Li-Jia Li, Kai Li, and Li Fei-Fei. Imagenet: A large-scale hierarchical image database. In *2009 IEEE conference on computer vision and pattern recognition*, pages 248–255. Ieee, 2009. [7](#), [8](#)

- [16] Jacob Devlin, Ming-Wei Chang, Kenton Lee, and Kristina Toutanova. Bert: Pre-training of deep bidirectional transformers for language understanding. pages 4171–4186, 2019. 1
- [17] Kevin Donnelly et al. Snomed-ct: The advanced terminology and coding system for ehealth. *Studies in health technology and informatics*, 121:279, 2006. 6
- [18] Alexey Dosovitskiy, Lucas Beyer, Alexander Kolesnikov, Dirk Weissenborn, Xiaohua Zhai, Thomas Unterthiner, Mostafa Dehghani, Matthias Minderer, Georg Heigold, Sylvain Gelly, et al. An image is worth 16x16 words: Transformers for image recognition at scale. *arXiv preprint arXiv:2010.11929*, 2020. 13
- [19] Leyuan Fang, Chong Wang, Shutao Li, Hossein Rabbani, Xiangdong Chen, and Zhimin Liu. Attention to lesion: Lesion-aware convolutional neural network for retinal optical coherence tomography image classification. *IEEE transactions on medical imaging*, 38(8):1959–1970, 2019. 3
- [20] Ivan Gonzalez-Diaz. Dermaknet: Incorporating the knowledge of dermatologists to convolutional neural networks for skin lesion diagnosis. *IEEE journal of biomedical and health informatics*, 23(2):547–559, 2018. 3
- [21] Yu Gu, Robert Tinn, Hao Cheng, Michael Lucas, Naoto Usuyama, Xiaodong Liu, Tristan Naumann, Jianfeng Gao, and Hoifung Poon. Domain-specific language model pretraining for biomedical natural language processing. *ACM Transactions on Computing for Healthcare (HEALTH)*, 3(1):1–23, 2021. 8, 12
- [22] Kaiming He, Xiangyu Zhang, Shaoqing Ren, and Jian Sun. Deep residual learning for image recognition. In *Proceedings of the IEEE conference on computer vision and pattern recognition*, pages 770–778, 2016. 5, 7, 13
- [23] Shih-Cheng Huang, Liyue Shen, Matthew P Lungren, and Serena Yeung. Gloria: A multimodal global-local representation learning framework for label-efficient medical image recognition. In *Proceedings of the IEEE/CVF International Conference on Computer Vision*, pages 3942–3951, 2021. Official Implementation: <https://github.com/marshuang80/gloria>. 1, 3, 7, 12
- [24] Xin Huang, Yu Fang, Mingming Lu, Fengqi Yan, Jun Yang, and Yilu Xu. Dual-ray net: automatic diagnosis of thoracic diseases using frontal and lateral chest x-rays. *Journal of Medical Imaging and Health Informatics*, 10(2):348–355, 2020. 3
- [25] Sarfaraz Hussein, Kunlin Cao, Qi Song, and Ulas Bagci. Risk stratification of lung nodules using 3d cnn-based multi-task learning. In *International conference on information processing in medical imaging*, pages 249–260. Springer, 2017. 3
- [26] Jeremy Irvin, Pranav Rajpurkar, Michael Ko, Yifan Yu, Silvana Ciurea-Ilcus, Chris Chute, Henrik Marklund, Behzad Haghgoo, Robyn Ball, Katie Shpanskaya, et al. Chexpert: A large chest radiograph dataset with uncertainty labels and expert comparison. In *Proceedings of the AAAI conference on artificial intelligence*, volume 33, pages 590–597, 2019. 2, 3, 7, 9
- [27] Saahil Jain, Ashwin Agrawal, Adriel Saporta, Steven Truong, Du Nguyen Duong, Tan Bui, Pierre Chambon, Yuhao Zhang, Matthew Lungren, Andrew Ng, Curtis Langlotz, Pranav Rajpurkar, and Pranav Rajpurkar. Radgraph: Extracting clinical entities and relations from radiology reports. In J. Vanschoren and S. Yeung, editors, *Proceedings of the Neural Information Processing Systems Track on Datasets and Benchmarks*, volume 1, 2021. URL <https://datasets-benchmarks-proceedings.neurips.cc/paper/2021/file/c8ffe9a587b126f152ed3d89a146b445-Paper-round1.pdf>. 3, 8, 9
- [28] Chao Jia, Yinfei Yang, Ye Xia, Yi-Ting Chen, Zarana Parekh, Hieu Pham, Quoc Le, Yun-Hsuan Sung, Zhen Li, and Tom Duerig. Scaling up visual and vision-language representation learning with noisy text supervision. In *International Conference on Machine Learning*, pages 4904–4916. PMLR, 2021. 3
- [29] Alistair EW Johnson, Tom J Pollard, Seth J Berkowitz, Nathaniel R Greenbaum, Matthew P Lungren, Chih-ying Deng, Roger G Mark, and Steven Horng. MIMIC-CXR, a de-identified publicly available database of chest radiographs with free-text reports. *Scientific data*, 6(1):1–8, 2019. 1, 6, 7, 8, 9

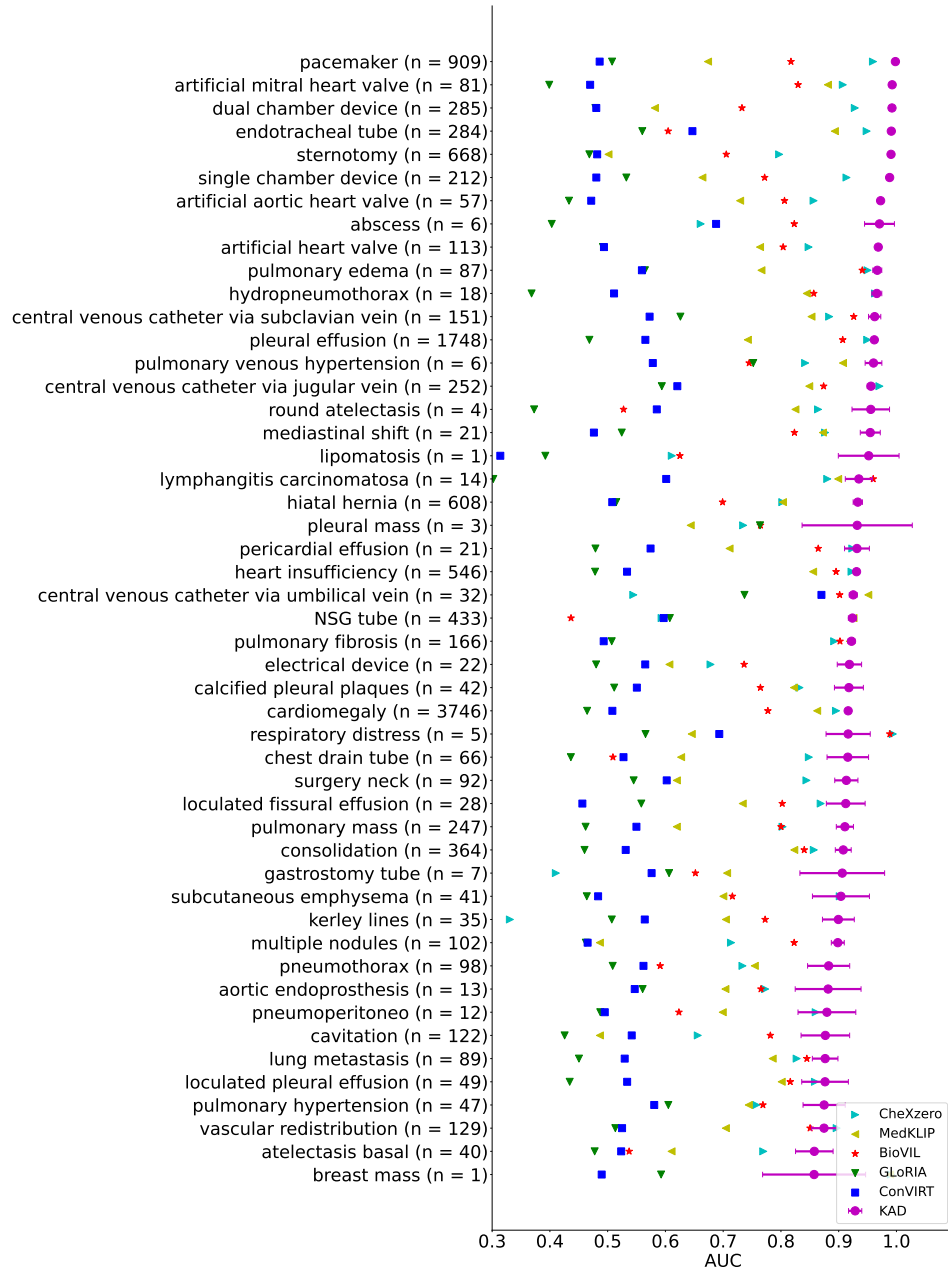
- [30] Junnan Li, Ramprasaath Selvaraju, Akhilesh Gotmare, Shafiq Joty, Caiming Xiong, and Steven Chu Hong Hoi. Align before fuse: Vision and language representation learning with momentum distillation. *Advances in neural information processing systems*, 34:9694–9705, 2021. 3
- [31] Liu Li, Mai Xu, Xiaofei Wang, Lai Jiang, and Hanruo Liu. Attention based glaucoma detection: a large-scale database and cnn model. In *Proceedings of the IEEE/CVF conference on computer vision and pattern recognition*, pages 10571–10580, 2019. 3
- [32] Liunian Harold Li, Mark Yatskar, Da Yin, Cho-Jui Hsieh, and Kai-Wei Chang. Visualbert: A simple and performant baseline for vision and language. *arXiv preprint arXiv:1908.03557*, 2019. 3
- [33] Xiaomeng Li, Xiaowei Hu, Lequan Yu, Lei Zhu, Chi-Wing Fu, and Pheng-Ann Heng. Canet: cross-disease attention network for joint diabetic retinopathy and diabetic macular edema grading. *IEEE transactions on medical imaging*, 39(5):1483–1493, 2019. 3
- [34] Qing Liao, Ye Ding, Zoe L Jiang, Xuan Wang, Chunkai Zhang, and Qian Zhang. Multi-task deep convolutional neural network for cancer diagnosis. *Neurocomputing*, 348:66–73, 2019. 3
- [35] Jingyu Liu, Jie Lian, and Yizhou Yu. Chestx-det10: Chest x-ray dataset on detection of thoracic abnormalities, 2020. 2, 7, 9
- [36] Ilya Loshchilov and Frank Hutter. Decoupled weight decay regularization. *arXiv preprint arXiv:1711.05101*, 2017. 8
- [37] Chaofan Ma, Yuhuan Yang, Yanfeng Wang, Ya Zhang, and Weidi Xie. Open-vocabulary semantic segmentation with frozen vision-language models. *arXiv preprint arXiv:2210.15138*, 2022. 1
- [38] Gabriel Maicas, Andrew P Bradley, Jacinto C Nascimento, Ian Reid, and Gustavo Carneiro. Training medical image analysis systems like radiologists. In *International Conference on Medical Image Computing and Computer-Assisted Intervention*, pages 546–554. Springer, 2018. 3
- [39] Matthew BA McDermott, Tzu Ming Harry Hsu, Wei-Hung Weng, Marzyeh Ghassemi, and Peter Szolovits. Chexpert++: Approximating the chexpert labeler for speed, differentiability, and probabilistic output. In *Machine Learning for Healthcare Conference*, pages 913–927. PMLR, 2020. 3
- [40] Masahiro Mitsuhara, Hiroshi Fukui, Yusuke Sakashita, Takanori Ogata, Tsubasa Hirakawa, Takayoshi Yamashita, and Hironobu Fujiyoshi. Embedding human knowledge into deep neural network via attention map. *arXiv preprint arXiv:1905.03540*, 2019. 3
- [41] Philip Müller, Georgios Kaissis, Congyu Zou, and Daniel Rückert. Joint learning of localized representations from medical images and reports. *arXiv preprint arXiv:2112.02889*, 2021. 1
- [42] Mark Neumann, Daniel King, Iz Beltagy, and Waleed Ammar. Scispacy: Fast and robust models for biomedical natural language processing. In *Proceedings of the 18th BioNLP Workshop and Shared Task*, pages 319–327. Association for Computational Linguistics, 2019. doi: 10.18653/v1/W19-5034. URL <https://aclanthology.org/W19-5034>. 8
- [43] Yifan Peng, Xiaosong Wang, Le Lu, Mohammadhadi Bagheri, Ronald Summers, and Zhiyong Lu. Negbio: a high-performance tool for negation and uncertainty detection in radiology reports. *AMIA Summits on Translational Science Proceedings*, 2018:188, 2018. 3
- [44] Alec Radford, Jong Wook Kim, Chris Hallacy, Aditya Ramesh, Gabriel Goh, Sandhini Agarwal, Girish Sastry, Amanda Askell, Pamela Mishkin, Jack Clark, et al. Learning transferable visual models from natural language supervision. In *International Conference on Machine Learning*, pages 8748–8763. PMLR, 2021. 1, 7
- [45] Pranav Rajpurkar, Anirudh Joshi, Anuj Pareek, Andrew Y Ng, and Matthew P Lungren. Chex-ternal: Generalization of deep learning models for chest x-ray interpretation to photos of chest x-rays and external clinical settings. In *Proceedings of the Conference on Health, Inference, and Learning*, pages 125–132, 2021. 7

- [46] Sheng Shen, Liunian Harold Li, Hao Tan, Mohit Bansal, Anna Rohrbach, Kai-Wei Chang, Zhewei Yao, and Kurt Keutzer. How much can clip benefit vision-and-language tasks? *arXiv preprint arXiv:2107.06383*, 2021. 1
- [47] Akshay Smit, Saahil Jain, Pranav Rajpurkar, Anuj Pareek, Andrew Y Ng, and Matthew Lungren. Combining automatic labelers and expert annotations for accurate radiology report labeling using bert. In *Proceedings of the 2020 Conference on Empirical Methods in Natural Language Processing (EMNLP)*, pages 1500–1519, 2020. 3
- [48] Jiaxing Tan, Yumei Huo, Zhengrong Liang, and Lihong Li. Expert knowledge-infused deep learning for automatic lung nodule detection. *Journal of X-ray Science and Technology*, 27(1): 17–35, 2019. 3
- [49] Ekin Tiu, Ellie Talius, Pujan Patel, Curtis P Langlotz, Andrew Y Ng, and Pranav Rajpurkar. Expert-level detection of pathologies from unannotated chest x-ray images via self-supervised learning. *Nature Biomedical Engineering*, pages 1–8, 2022. 7, 9
- [50] Ashish Vaswani, Noam Shazeer, Niki Parmar, Jakob Uszkoreit, Llion Jones, Aidan N Gomez, Lukasz Kaiser, and Illia Polosukhin. Attention is all you need. *Advances in neural information processing systems*, 30, 2017. 8
- [51] David Wadden, Ulme Wennberg, Yi Luan, and Hannaneh Hajishirzi. Entity, relation, and event extraction with contextualized span representations. *arXiv preprint arXiv:1909.03546*, 2019.
- [52] Kun Wang, Xiaohong Zhang, Sheng Huang, Feiyu Chen, Xiangbo Zhang, and Luwen Huangfu. Learning to recognize thoracic disease in chest x-rays with knowledge-guided deep zoom neural networks. *IEEE Access*, 8:159790–159805, 2020. 3
- [53] Xiaosong Wang, Yifan Peng, Le Lu, Zhiyong Lu, Mohammadhadi Bagheri, and Ronald M Summers. Chestx-ray8: Hospital-scale chest x-ray database and benchmarks on weakly-supervised classification and localization of common thorax diseases. In *Proceedings of the IEEE conference on computer vision and pattern recognition*, pages 2097–2106, 2017. 2, 7, 9
- [54] Chaoyi Wu, Xiaoman Zhang, Yanfeng Wang, Ya Zhang, and Weidi Xie. K-diag: Knowledge-enhanced disease diagnosis in radiographic imaging, 2023. 3
- [55] Chaoyi Wu, Xiaoman Zhang, Ya Zhang, Yanfeng Wang, and Weidi Xie. Medklip: Medical knowledge enhanced language-image pre-training. *medRxiv*, 2023. 3, 7
- [56] Joy T Wu, Nkechinyere Nneka Agu, Ismini Lourentzou, Arjun Sharma, Joseph Alexander Paguio, Jasper Seth Yao, Edward Christopher Dee, William G Mitchell, Satyananda Kashyap, Andrea Giovannini, et al. Chest imagenome dataset for clinical reasoning. In *Thirty-fifth Conference on Neural Information Processing Systems Datasets and Benchmarks Track (Round 2)*, 2021. 3
- [57] Xiaozheng Xie, Jianwei Niu, Xuefeng Liu, Zhongsu Chen, Shaojie Tang, and Shui Yu. A survey on incorporating domain knowledge into deep learning for medical image analysis. *Medical Image Analysis*, 69:101985, 2021. 3
- [58] Yutong Xie, Yong Xia, Jianpeng Zhang, Yang Song, Dagan Feng, Michael Fulham, and Weidong Cai. Knowledge-based collaborative deep learning for benign-malignant lung nodule classification on chest ct. *IEEE transactions on medical imaging*, 38(4):991–1004, 2018. 3
- [59] Wenkai Yang, Juanjuan Zhao, Yan Qiang, Xiaotang Yang, Yunyun Dong, Qianqian Du, Guohua Shi, and Muhammad Bilal Zia. Dscgans: Integrate domain knowledge in training dual-path semi-supervised conditional generative adversarial networks and s3vm for ultrasonography thyroid nodules classification. In *International conference on medical image computing and computer-assisted intervention*, pages 558–566. Springer, 2019. 3
- [60] Jianming Zhang, Sarah Adel Bargal, Zhe Lin, Jonathan Brandt, Xiaohui Shen, and Stan Sclaroff. Top-down neural attention by excitation backprop. *International Journal of Computer Vision*, 126(10):1084–1102, 2018. 9

- [61] Yuhao Zhang, Hang Jiang, Yasuhide Miura, Christopher D Manning, and Curtis P Langlotz. Contrastive learning of medical visual representations from paired images and text. In *Machine Learning for Healthcare*, 2022. Highest Starred Implementation: <https://github.com/edreisMD/ConVIRT-pytorch>. 1, 3, 7
- [62] Hong-Yu Zhou, Shuang Yu, Cheng Bian, Yifan Hu, Kai Ma, and Yefeng Zheng. Comparing to learn: Surpassing imagenet pretraining on radiographs by comparing image representations. In *International Conference on Medical Image Computing and Computer-Assisted Intervention*, pages 398–407. Springer, 2020. 7, 8
- [63] Hong-Yu Zhou, Xiaoyu Chen, Yinghao Zhang, Ruibang Luo, Liansheng Wang, and Yizhou Yu. Generalized radiograph representation learning via cross-supervision between images and free-text radiology reports. *Nature Machine Intelligence*, 4(1):32–40, 2022. 1
- [64] Zongwei Zhou, Vatsal Sodha, Jiaxuan Pang, Michael B Gotway, and Jianming Liang. Models genesis. *Medical image analysis*, 67:101840, 2021. 7, 8



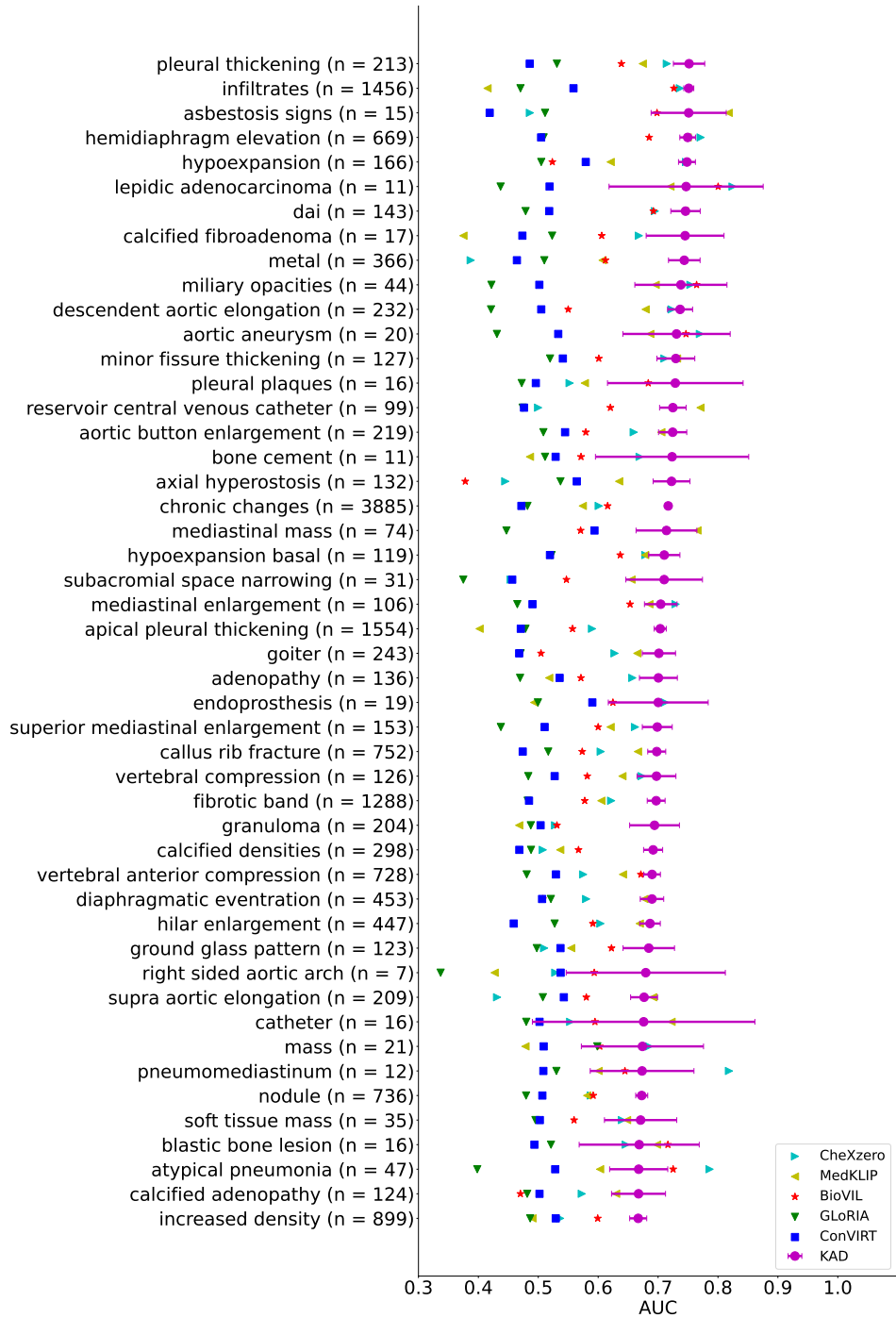
Supplementary Fig. 7: Dataset distribution of PadChest (39053 manually labeled samples). It can be observed that only 21 classes have more than 1000 samples and the data tend to show a long-tailed distribution.



Supplementary Fig. 8: Comparison of KAD with SOTA medical image-text pre-training models on the 174 different radiographic findings and 19 differential diagnosis, totaling 193 classes. We evaluate model on the human-annotated subset of the PadChest dataset ($n = 39,053$ chest X-rays) under **zero-shot** setting. Here we show the results of the results for the **1-49** classes. Mean AUC and 95% CI of KAD are shown for each class, and n refers to the number of positive samples.



Supplementary Fig. 9: Comparison of KAD with SOTA medical image-text pre-training models on the 174 different radiographic findings and 19 differential diagnosis, totaling 193 classes. We evaluate model on the human-annotated subset of the PadChest dataset ($n = 39,053$ chest X-rays) under **zero-shot** setting. Here we show the results of the results for the **50-97** classes. Mean AUC and 95% CI of KAD are shown for each class, and n refers to the number of positive samples.



Supplementary Fig. 10: Comparison of KAD with SOTA medical image-text pre-training models on the 174 different radiographic findings and 19 differential diagnosis, totaling 193 classes. We evaluate model on the human-annotated subset of the PadChest dataset ($n = 39,053$ chest X-rays) under **zero-shot** setting. Here we show the results of the results for the **98-145** classes. Mean AUC and 95% CI of KAD are shown for each class, and n refers to the number of positive samples.



Supplementary Fig. 11: Comparison of KAD with SOTA medical image-text pre-training models on the 174 different radiographic findings and 19 differential diagnosis, totaling 193 classes. We evaluate model on the human-annotated subset of the PadChest dataset ($n = 39,053$ chest X-rays) under **zero-shot** setting. Here we show the results of the results for the **146-193** classes. Mean AUC and 95% CI of KAD are shown for each class, and n refers to the number of positive samples.

Supplementary Table 3: Comparison with other state-of-the-art medical image-text pre-training methods on **zero-shot** classification task on ChestX-ray14.

Metric	Method	Mean	Atelectasis	Cardiomegaly	Effusion	Infiltration	Mass	Nodule	Pneumonia	Pneumothorax	Consolidation	Edema	Emphysema	Fibrosis	Pleural Thicken	Hernia
AUC	ConVIRT	0.560	0.459	0.433	0.646	0.654	0.601	0.580	0.640	0.533	0.646	0.692	0.431	0.482	0.545	0.494
	GLoRIA	0.610	0.653	0.704	0.762	0.660	0.613	0.508	0.587	0.572	0.697	0.762	0.499	0.459	0.613	0.450
	BioViL	0.662	0.517	0.688	0.743	0.601	0.663	0.639	0.669	0.683	0.650	0.795	0.656	0.632	0.637	0.698
	MedKLIP	0.726	0.671	0.842	0.813	0.706	0.742	0.621	0.698	0.821	0.719	0.803	0.783	0.604	0.499	0.841
	KAD	0.789	0.770	0.854	0.824	0.694	0.754	0.698	0.734	0.860	0.718	0.809	0.879	0.780	0.718	0.952
	(95% CI)	0.770	0.750	0.839	0.816	0.679	0.736	0.676	0.712	0.850	0.703	0.780	0.866	0.752	0.698	0.917
	0.808	0.790	0.869	0.832	0.709	0.772	0.719	0.756	0.870	0.733	0.838	0.892	0.808	0.740	0.986	
MCC	ConVIRT	0.074	0.004	0.013	0.182	0.207	0.100	0.071	0.066	0.079	0.113	0.119	0.012	0.009	0.049	0.014
	GLoRIA	0.108	0.157	0.126	0.313	0.210	0.087	0.021	0.044	0.095	0.156	0.167	0.032	0.008	0.076	0.016
	BioViL	0.133	0.056	0.173	0.289	0.138	0.124	0.102	0.076	0.180	0.138	0.207	0.102	0.058	0.086	0.124
	MedKLIP	0.197	0.171	0.273	0.396	0.282	0.203	0.106	0.092	0.371	0.190	0.199	0.238	0.066	0.018	0.154
	KAD	0.280	0.293	0.344	0.419	0.270	0.237	0.155	0.114	0.445	0.174	0.200	0.389	0.149	0.142	0.582
	(95% CI)	0.248	0.258	0.302	0.400	0.246	0.206	0.125	0.098	0.420	0.159	0.180	0.373	0.122	0.125	0.463
	0.312	0.328	0.386	0.438	0.294	0.268	0.185	0.129	0.469	0.188	0.219	0.424	0.175	0.158	0.700	
F1	ConVIRT	0.135	0.001	0.002	0.367	0.436	0.157	0.142	0.060	0.205	0.177	0.121	0.083	0.034	0.097	0.007
	GLoRIA	0.174	0.281	0.167	0.452	0.442	0.155	0.122	0.053	0.209	0.200	0.146	0.086	0.004	0.109	0.007
	BioViL	0.192	0.235	0.209	0.438	0.414	0.178	0.164	0.067	0.274	0.177	0.187	0.123	0.056	0.119	0.045
	MedKLIP	0.244	0.292	0.301	0.516	0.483	0.256	0.175	0.076	0.438	0.218	0.173	0.246	0.079	0.010	0.154
	KAD	0.323	0.392	0.359	0.534	0.475	0.296	0.210	0.086	0.499	0.196	0.170	0.424	0.128	0.163	0.580
	(95% CI)	0.294	0.363	0.318	0.518	0.459	0.266	0.181	0.074	0.478	0.185	0.151	0.399	0.106	0.150	0.462
	0.351	0.420	0.400	0.550	0.490	0.326	0.238	0.098	0.520	0.207	0.188	0.448	0.150	0.175	0.698	
ACC	ConVIRT	0.459	0.872	0.958	0.504	0.632	0.389	0.494	0.520	0.266	0.548	0.661	0.063	0.029	0.354	0.132
	GLoRIA	0.503	0.466	0.919	0.674	0.613	0.447	0.183	0.482	0.279	0.586	0.694	0.183	0.982	0.466	0.072
	BioViL	0.633	0.218	0.904	0.678	0.403	0.571	0.644	0.604	0.648	0.437	0.790	0.615	0.747	0.601	0.997
	MedKLIP	0.796	0.520	0.919	0.799	0.672	0.809	0.825	0.671	0.837	0.607	0.754	0.858	0.924	0.954	0.993
	KAD	0.816	0.799	0.956	0.802	0.671	0.878	0.896	0.742	0.862	0.461	0.733	0.952	0.906	0.768	0.997
	(95% CI)	0.810	0.790	0.952	0.796	0.660	0.871	0.890	0.738	0.855	0.455	0.724	0.949	0.899	0.759	0.996
	0.822	0.807	0.959	0.807	0.681	0.885	0.901	0.747	0.869	0.467	0.741	0.955	0.912	0.777	0.998	

AUC, MCC, F1 and ACC scores are reported, and the metrics all refer to the macro average on all the diseases. Numbers within the last two rows indicate 95% CI. The best results are bold.

Supplementary Table 4: Comparison with other state-of-the-art medical image-text pre-training and self-supervised learning methods on fine-tuning classification task on ChestX-ray14.

Training data	Method	Mean	Atelectasis	Cardiomegaly	Effusion	Infiltration	Mass	Nodule	Pneumonia	Pneumothorax	Consolidation	Edema	Emphysema	Fibrosis	Pleural Thicken	Hernia
1%	ResNet-50	0.581	0.557	0.577	0.636	0.616	0.550	0.602	0.571	0.582	0.608	0.633	0.534	0.637	0.568	0.460
	ConVIRT	0.649	0.660	0.782	0.789	0.611	0.596	0.655	0.608	0.688	0.657	0.607	0.658	0.680	0.627	0.466
	GLoRIA	0.597	0.597	0.567	0.741	0.646	0.559	0.557	0.611	0.607	0.665	0.669	0.550	0.558	0.592	0.436
	BioViL	0.579	0.555	0.564	0.722	0.650	0.567	0.546	0.626	0.560	0.657	0.681	0.516	0.513	0.592	0.360
	MG	0.595	0.604	0.741	0.705	0.608	0.514	0.597	0.557	0.544	0.645	0.670	0.505	0.669	0.581	0.395
	C2L	0.613	0.650	0.644	0.753	0.640	0.572	0.585	0.632	0.540	0.654	0.706	0.496	0.634	0.593	0.485
	ImageNet	0.635	0.662	0.642	0.721	0.570	0.590	0.585	0.600	0.626	0.624	0.668	0.615	0.707	0.631	0.645
	MedKLIP	0.609	0.655	0.590	0.745	0.643	0.550	0.611	0.609	0.599	0.659	0.682	0.535	0.648	0.593	0.400
	KAD	0.787	0.770	0.882	0.829	0.692	0.751	0.697	0.735	0.861	0.727	0.813	0.893	0.743	0.692	0.938
10%	ResNet-50	0.691	0.682	0.766	0.746	0.674	0.623	0.580	0.636	0.728	0.678	0.780	0.647	0.715	0.653	0.771
	ConVIRT	0.771	0.740	0.843	0.811	0.693	0.748	0.700	0.671	0.828	0.701	0.814	0.871	0.767	0.719	0.893
	GLoRIA	0.743	0.721	0.808	0.800	0.687	0.733	0.675	0.658	0.779	0.676	0.797	0.799	0.787	0.693	0.787
	BioViL	0.727	0.703	0.785	0.790	0.666	0.718	0.671	0.665	0.767	0.684	0.799	0.761	0.748	0.653	0.763
	MG	0.703	0.697	0.798	0.774	0.663	0.666	0.594	0.604	0.708	0.682	0.770	0.645	0.735	0.665	0.841
	C2L	0.732	0.714	0.834	0.789	0.684	0.687	0.654	0.631	0.786	0.701	0.794	0.774	0.742	0.679	0.776
	ImageNet	0.726	0.709	0.798	0.769	0.684	0.693	0.656	0.630	0.793	0.671	0.767	0.749	0.729	0.711	0.810
	MedKLIP	0.748	0.729	0.802	0.793	0.698	0.719	0.681	0.666	0.796	0.696	0.811	0.795	0.756	0.713	0.819
	KAD	0.807	0.776	0.889	0.833	0.718	0.783	0.719	0.737	0.872	0.750	0.833	0.903	0.807	0.723	0.953
100%	ResNet-50	0.790	0.750	0.879	0.815	0.691	0.798	0.726	0.703	0.826	0.731	0.839	0.835	0.807	0.754	0.903
	ConVIRT	0.808	0.771	0.867	0.825	0.703	0.818	0.761	0.722	0.857	0.747	0.854	0.901	0.809	0.771	0.909
	GLoRIA	0.800	0.760	0.855	0.818	0.700	0.814	0.749	0.715	0.828	0.739	0.832	0.887	0.813	0.767	0.921
	BioViL	0.800	0.765	0.871	0.824	0.697	0.819	0.752	0.710	0.845	0.742	0.842	0.871	0.821	0.759	0.888
	MG	0.777	0.737	0.866	0.812	0.677	0.786	0.674	0.689	0.806	0.733	0.834	0.833	0.797	0.744	0.892
	C2L	0.802	0.766	0.865	0.824	0.688	0.810	0.758	0.712	0.845	0.744	0.830	0.889	0.811	0.763	0.925
	ImageNet	0.804	0.763	0.867	0.823	0.693	0.823	0.763	0.719	0.840	0.737	0.842	0.893	0.819	0.770	0.899
	MedKLIP	0.801	0.764	0.849	0.823	0.697	0.820	0.747	0.712	0.839	0.751	0.848	0.879	0.817	0.777	0.892
	KAD	0.825	0.785	0.897	0.840	0.713	0.836	0.771	0.740	0.874	0.753	0.860	0.916	0.829	0.778	0.961

AUC scores are reported, and the metrics all refer to the macro average on all the diseases. The best results are bold. MG refers to “Model Genesis”. ImageNet refers to “ImageNet Pre-training”.

Supplementary Table 5: Comparisons of proposed KAD with SOTA medical image-text pre-training models and three board-certified radiologists on five competition pathologies in CheXpert dataset.

	Mean	Atelectasis	Cardiomegaly	Consolidation	Edema	Pleural effusion
AUC						
ConVIRT	0.590 (0.557,0.624)	0.524 (0.512,0.536)	0.548 (0.525,0.571)	0.680 (0.630,0.730)	0.582 (0.537,0.626)	0.618 (0.580,0.656)
GLoRIA	0.750 (0.711,0.789)	0.807 (0.779,0.836)	0.802 (0.781,0.823)	0.588 (0.540,0.635)	0.747 (0.687,0.806)	0.807 (0.769,0.846)
BioVIL	0.693 (0.651,0.736)	0.637 (0.604,0.671)	0.694 (0.671,0.716)	0.705 (0.636,0.774)	0.638 (0.601,0.675)	0.793 (0.743,0.844)
CheXzero	0.889 (0.849,0.922)	0.816 (0.777,0.852)	0.906 (0.876,0.930)	0.892 (0.823,0.947)	0.897 (0.864,0.928)	0.932 (0.906,0.955)
MedKLIP	0.879 (0.855,0.903)	0.813 (0.790,0.835)	0.866 (0.842,0.890)	0.858 (0.821,0.895)	0.911 (0.890,0.931)	0.947 (0.931,0.963)
KAD	0.905 (0.886,0.924)	0.884 (0.863,0.904)	0.885 (0.866,0.904)	0.865 (0.837,0.893)	0.943 (0.928,0.958)	0.949 (0.935,0.963)
MCC						
Radiologists(mean)	0.530 (0.499,0.558)	0.548 (0.496,0.606)	0.566 (0.511,0.620)	0.359 (0.262,0.444)	0.507 (0.431,0.570)	0.548 (0.496,0.606)
ConVIRT	0.231 (0.150,0.313)	0.180 (0.132,0.229)	0.146 (0.081,0.211)	0.315 (0.225,0.405)	0.280 (0.154,0.405)	0.236 (0.159,0.314)
GLoRIA	0.501 (0.419,0.584)	0.550 (0.502,0.598)	0.610 (0.568,0.651)	0.275 (0.142,0.408)	0.443 (0.313,0.574)	0.628 (0.567,0.688)
BioVIL	0.368 (0.297,0.438)	0.249 (0.191,0.306)	0.439 (0.379,0.499)	0.252 (0.165,0.340)	0.403 (0.332,0.474)	0.495 (0.419,0.571)
CheXzero	0.523 (0.486,0.561)	0.468 (0.396,0.541)	0.625 (0.553,0.700)	0.374 (0.290,0.458)	0.520 (0.424,0.616)	0.628 (0.558,0.696)
MedKLIP	0.540 (0.476,0.603)	0.476 (0.434,0.517)	0.574 (0.522,0.625)	0.404 (0.295,0.512)	0.563 (0.502,0.623)	0.683 (0.627,0.739)
KAD	0.589 (0.536,0.642)	0.613 (0.567,0.659)	0.607 (0.558,0.656)	0.357 (0.293,0.421)	0.666 (0.608,0.724)	0.702 (0.653,0.751)
F1						
Radiologists(mean)	0.619 (0.585,0.642)	0.692 (0.646,0.731)	0.678 (0.634,0.718)	0.385 (0.280,0.485)	0.583 (0.511,0.645)	0.737 (0.689,0.783)
ConVIRT	0.264 (0.187,0.342)	0.090 (0.045,0.135)	0.234 (0.176,0.292)	0.353 (0.261,0.444)	0.272 (0.151,0.393)	0.373 (0.301,0.445)
GLoRIA	0.570 (0.498,0.643)	0.668 (0.636,0.699)	0.713 (0.675,0.751)	0.269 (0.145,0.393)	0.511 (0.391,0.630)	0.691 (0.641,0.742)
BioVIL	0.463 (0.408,0.518)	0.496 (0.461,0.531)	0.545 (0.505,0.585)	0.276 (0.204,0.347)	0.407 (0.327,0.487)	0.590 (0.542,0.639)
CheXzero	0.606 (0.571,0.638)	0.646 (0.593,0.700)	0.743 (0.685,0.793)	0.333 (0.239,0.424)	0.602 (0.517,0.678)	0.704 (0.634,0.764)
MedKLIP	0.614 (0.555,0.673)	0.624 (0.589,0.658)	0.694 (0.656,0.732)	0.415 (0.300,0.529)	0.601 (0.541,0.661)	0.738 (0.689,0.787)
KAD	0.646 (0.591,0.702)	0.720 (0.681,0.758)	0.721 (0.684,0.757)	0.342 (0.237,0.447)	0.701 (0.647,0.754)	0.748 (0.705,0.792)

Note that, all models are directly evaluated on CheXpert dataset under **zero-shot** setting. Numbers within parentheses indicate 95% CI. The best results are bold.

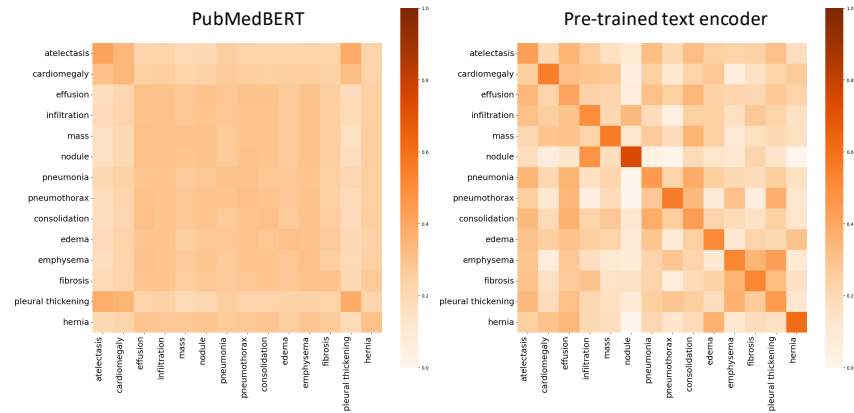
Supplementary Table 6: Comparisons of proposed KAD with SOTA medical image-text pre-training models on zero-shot classification and grounding task in ChestX-Det10 dataset.

Metric	Method	Mean	Atelectasis	Calcification	Consolidation	Effusion	Emphysema	Fibrosis	Fracture	Mass	Nodule	Pneumothorax
AUC	GLoRIA	0.645	0.622	0.524	0.718	0.866	0.607	0.523	0.494	0.725	0.63	0.744
	BioViL	0.663	0.617	0.521	0.808	0.789	0.78	0.607	0.623	0.612	0.591	0.686
	KAD	0.735	0.757	0.563	0.824	0.888	0.888	0.687	0.608	0.695	0.566	0.874
	KAD-512	0.771	0.812	0.578	0.854	0.892	0.916	0.671	0.666	0.703	0.705	0.913
	KAD-1024	0.764	0.793	0.661	0.789	0.861	0.880	0.684	0.606	0.680	0.763	0.923
Pointing Game	GLoRIA	0.367	0.479	0.053	0.737	0.528	0.667	0.366	0.013	0.533	0.156	0.143
	BioViL	0.380	0.375	0.105	0.664	0.615	0.795	0.378	0.013	0.500	0.130	0.229
	KAD	0.391	0.646	0.132	0.699	0.618	0.644	0.244	0.199	0.267	0.316	0.143
	KAD-512	0.462	0.729	0.158	0.713	0.738	0.769	0.293	0.237	0.433	0.377	0.171
	KAD-1024	0.485	0.771	0.316	0.692	0.560	0.718	0.379	0.132	0.367	0.571	0.343

AUC scores are shown for the zero-shot classification task, and Pointing game scores are shown for the zero-shot grounding task. Note that, all models are directly evaluated on ChestX-Det10 dataset under **zero-shot** setting. The best results are bold.

Supplementary Table 7: Entity set Q . We select top $Q = 40$ most commonly appearing entities in the report corpus.

pleural effusion	opacity	pneumothorax	edema
atelectasis	tube	consolidation	enlarged cardiomediastinum
tip	pneumonia	line	cardiomegaly
fracture	calcification	device	engorgement
nodule	wire	pacemaker	pleural thicken
marking	scar	hyperinflate	blunt
collapse	emphysema	aerate	mass
infiltration	obscure	deformity	hernia
drainage	distention	shift	normal
lesion	hardware	dilation	aspiration



Supplementary Fig. 12: Similarity map between features of different disease names encoded by PubMedBERT and Med-KEBERT.